Turun yliopisto
University of Turku

BIOIMAGE INFORMATICS IN STED SUPER-RESOLUTION MICROSCOPY

Sami Koho

TURUN YLIOPISTON JULKAISUJA – ANNALES UNIVERSITATIS TURKUENSIS
Sarja - ser. D osa - tom. 1219 | Medica - Odontologica | Turku 2016

University of Turku

Faculty of Medicine
Institute of Biomedicine
Department of Cell Biology and Anatomy
Laboratory of Biophysics
University of Turku Doctoral Programme of Molecular Medicine (TuDMM)

Supervised by

Professor Pekka Hänninen Ph.D.
Laboratory of Biophysics
Department of Cell Biology and Anatomy
University of Turku
Turku, Finland

Reviewed by

Assoc. Professor Juha Toivonen, PhD
Department of Physics
Tampere University of Technology
Tampere, Finland

Professor Ulla Ruotsalainen, PhD.
Institute of Signal Processing
Tampere University of Technology
Tampere, Finland

Opponent

Dr. Giuseppe Vicidomini
Department of Nanophysics
Italian Institute of Technology
Genoa, Italy

The originality of this thesis has been checked in accordance with the University of Turku quality assurance system using the Turnitin OriginalityCheck service.

ISBN 978-951-29-6391-1 (PRINT)
ISBN 978-951-29-6392-8 (PDF)
ISSN 0355-9483
Painosalama Oy - Turku, Finland 2016

"If you don't overestimate your abilities several times over, you just see dangers, not possibilities. If you doubt your abilities, you'll never improve"

- Magnus Carlsen, a Chess world champion

Sami Koho

Bioimage informatics in STED super-resolution microscopy

University of Turku, Faculty of Medicine, Institute of Biomedicine, Department of Cell Biology and Anatomy, Laboratory of Biophysics
University of Turku Doctoral Programme in Molecular Medicine (TuDMM)
Annales Universitatis Turkuensis, Medica – Odontologica, Painosalama Oy, Turku 2016

ABSTRACT

Optical microscopy is living its renaissance. The diffraction limit, although still physically true, plays a minor role in the achievable resolution in far-field fluorescence microscopy. Super-resolution techniques enable fluorescence microscopy at nearly molecular resolution. Modern (super-resolution) microscopy methods rely strongly on software. Software tools are needed all the way from data acquisition, data storage, image reconstruction, restoration and alignment, to quantitative image analysis and image visualization. These tools play a key role in all aspects of microscopy today – and their importance in the coming years is certainly going to increase, when microscopy little-by-little transitions from single cells into more complex and even living model systems.

In this thesis, a series of bioimage informatics software tools are introduced for STED super-resolution microscopy. Tomographic reconstruction software, coupled with a novel image acquisition method STED< is shown to enable axial (3D) super-resolution imaging in a standard 2D-STED microscope. Software tools are introduced for STED super-resolution correlative imaging with transmission electron microscopes or atomic force microscopes. A novel method for automatically ranking image quality within microscope image datasets is introduced, and it is utilized to for example select the best images in a STED microscope image dataset.

Sami Koho

Biokuvantamisen informatiikkaa STED super-resoluutio mikroskopiassa

Turun yliopisto, Lääketieteellinen tiedekunta, Biolääketieteen laitos, Solubiologian ja anatomian oppiaine, Biofysiikan laboratorio
Molekyylilääketieteen tohtoriohjelma (TuDMM)
Annales Universitatis Turkuensis, Medica – Odontologica, Painosalama Oy, Turku 2016

TIIVISTELMÄ

On optisen mikroskopian renessanssin aika. Diffraktioraja ei enää käytännössä rajoita optisten mikroskooppien erottelukykyä, vaan ns. super-resoluutio fluoresenssimikroskooppitekniikoilla se voidaan ulottaa lähes yksittäisien molekyylien tasolle. Modernit mikroskooppitekniikat tukeutuvat voimakkaasti ohjelmistotyökaluihin: niiden avulla ohjataan mikroskooppeja, huolehditaan datan varastoinnista, muodostetaan kuvia laskennallisesti esim. kerroskuvausmenetelmin, korjataan kuvissa olevia virheitä esim. geometrisin muunnoksin tai dekonvoluutiomenetelmillä, sekä analysoidaan kuvia numeerisesti. Ohjelmistotyökaluilla on siis hyvin keskeinen asema tämän päivän mikroskooppitekniikoissa ja niiden merkitys tulee tulevaisuudessa ennestään kasvamaan, kun mikroskoopeilla yksittäisten solujen sijaan aletaan kuvata monimutkaisempia biologisia malleja.

Tämän väitöskirjan aiheena oli ohjelmistotyökalujen kehittäminen STED super-resoluutio mikroskopiatekniikan sovelluksiin. Uutta STED< datankeruutekniikkaa, sekä kerroskuvausmenetelmiä hyväksi käyttäen onnistuimme muodostamaan kuvia tavallisella 2D-STED mikroskoopilla, joiden resoluutio kaikissa kolmessa ulottuvuudessa on selvästi diffraktiorajaa parempi. Kehitimme ohjelmistotyökaluja, jotka mahdollistavat STED mikroskoopin korrelatiivisen käytön atomivoimamikroskoopin tai elektronimikroskoopin kanssa. Lisäksi kehitimme uuden ohjelmistotyökalun, joka pystyy automaattisesti arvioimaan mikroskooppikuvien laatua.

TABLE OF CONTENTS

ABBREVIATIONS

2D	Two-dimensional
3D	Three-dimensional
API	Application Programming Interface
CLEM	Correlative Light and Electron Microscopy
EM	Electron Microscope
FOV	Field Of View: the part of the sample that is visible through the microscope objective
FPALM	Fluorescence Photo-Activation Localization Microscopy
GPU	Graphics Processing Unit
GUI	Graphical User Interface
HCS	High Content Screening
I/O	Input/Output
iPALM	interferometric Photoactivated Localization Microscopy
LM	Light Microscope
ML	Maximum Likelihood
MMI	Mattes Mutual Information
MS	Mean-Squared difference
NA	Numerical aperture
NCC	Normalized Cross-Correlation
ND	Nanodiamond

OTF	Optical Transfer Function: the Fourier transformed PSF
PALM	Photoactivated Localization Microscopy
PMT	Photomultiplier tube
PSF	Point Spread Function: the impulse response of a microscope system
RESOLFT	REversible Saturable OpticaL Fluorescence Transitions
ROI	Region Of Interest
SIM	Structured illumination microscopy
SNR	Signal-To-Noise ratio
SPIM	Selective Plane Illumination Microscopy
STED	Stimulated Emission Depletion
STORM	Stochastic Optical Reconstruction Microscopy
TEM	Transmission Electron Microscope
TIRF	Total internal reflection fluorescence

LIST OF ORIGINAL PUBLICATIONS

I. Deguchi, T., Koho, S., Näreoja, T. & Hänninen, P. (2014) Axial super-resolution by mirror-reflected stimulated emission depletion microscopy. *Optical Review*, **21**, 389–394.

II. Koho, S., Deguchi, T. & Hänninen, P.E. (2015) A software tool for tomographic axial superresolution in STED microscopy. *Journal of Microscopy*, **2**, 208-218.

III. Koho, S., Deguchi, T., Löhmus, M., Näreoja, T. & Hänninen, P.E. (2015) A software tool for STED-AFM correlative super-resolution microscopy. *Proceedings of SPIE*, p. 93301K–93301K–7.

IV. Koho, S., Fazeli, E. & Hänninen, P. (2015) Image Quality Ranking Method for Microscopy, submitted manuscript.

In addition, some unpublished results are presented.

1. INTRODUCTION

Optical microscopy is living its renaissance. The diffraction limit, although still physically true, plays a minor role in the achievable resolution in far-field fluorescence microscopy. Super-resolution techniques enable fluorescence microscopy at nearly molecular resolution (Schmidt *et al.* 2008; Shtengel *et al.* 2009). Large, even partially opaque samples can be imaged (Swoger *et al.* 2007; Krzic 2009; Krzic *et al.* 2012) – sometimes even in real-time (Abrahamsson *et al.* 2013), at sub-diffraction resolution (Chen *et al.* 2014). The new microscopy techniques have allowed the realization of ambitious early biological applications (Keller *et al.* 2011; Wang *et al.* 2014; Chen *et al.* 2014) – however much remains to be seen, as these techniques are still being developed, and time is required to properly take full advantage of them.

Modern (super-resolution) microscopy methods rely strongly on software. Computational methods are needed all the way from data acquisition (*Chapters 2.1, 2.2*), data storage, image reconstruction, restoration and alignment (*Chapters 2.1.5, 2.2, 2.3, 2.4*), to quantitative image analysis (*Chapter 2.5*) and image visualization. Data acquisition software is used to capture microscope images – the complexity of such software may vary from simple frame grabbing functionality to complete instrument automation (Conrad *et al.* 2011). In correlative microscopy experiments, the data acquisition software may need to control several separate instruments, or at least a method to correlate the multi-modal images needs to be established at the post-processing stage (*Chapter 2.4*). Several modern microscopy techniques, such as localization super-resolution (*Chapter 2.2*), structured illumination (*Chapter 2.2*) and tomographic methods (*Chapter 2.3*) require image reconstruction in order to produce the intended image. The analysis of large datasets of biological images that are being produced with the modern microscopes requires the development of software for automated quantitative im-

age analysis (*Chapter 2.5*).

Because software development is in such a central role in today's microscopy experiments, it has recently evolved into a scientific discipline of its own, called bioimage informatics (Myers 2012). Bioimage informatics is a specialization of bioinformatics, specifically focused on microscopic biological imaging. An extensive review of the various aspects of bioimage informatics can be found in (Eliceiri *et al.* 2012).

In this Thesis, a series of bioimage informatics software tools are introduced for STED super-resolution microscopy. The developed tools cover bioimage informatics, from data acquisition, to image reconstruction, correlation and automated data analysis. Axial tomographic reconstruction software (**II**), coupled with a novel image acquisition method STED< (**I**) is shown to enable axial (3D) super-resolution imaging in a standard 2D-STED microscope. Software tools (**III** & (Prabhakar *et al.* Unpublished)**)** are introduced for STED super-resolution correlative imaging with atomic force microscopes or electron microscopes. A novel method for automatically ranking image quality within microscope image datasets is introduced (**IV**), and it is utilized to for example select the highest quality images in a STED microscope image dataset. All of the developed software has been made available under an open-source license, according to common scientific practices of bioimage informatics.

2. BACKGROUND

2.1. Fundamental concepts in fluorescence microscopy

Every microscope system distorts the image of the sample object in its own specific manner. Only by knowing the limitations, one can choose the correct microscope system for an experiment, and configure it in a way to ensure that all the available information is digitized – the Nyquist sampling theorem holds true in imaging as well, both in space and in time. Bioimage processing software can, to some extent be used to correct the distortions created by the microscope, but this assumes that proper data acquisition settings are used, passed on to the restoration algorithms, and that the point spread function of the microscope is known or can be estimated. In this chapter essential concepts in fluorescence microscopy are outlined, which serves as a foundation for the specialized subjects that follow.

2.1.1. Image acquisition

Fluorescence microscopy techniques can be roughly divided into two categories, based on the method they employ to acquire images. In wide-field microscopes (*Figure 1A*) the entire field-of-view (FOV) is illuminated as evenly as possible with unfocused excitation light (Köhler illumination), after which the fluorescence signal from the desired sample layer is recorded with a camera or observed by the eye. This allows capturing the whole FOV at once, and thus the imaging speed is only limited by the frame-rate of the camera and the amount of fluorescence signal desired for each frame. In raster-scanning microscopes (*Figure 1B*) the fluorescence excitation light is focused typically to a single point – the fluorescence signal is recorded in a sequential manner, one sampling position at a time, which requires the implementation of a method for precisely moving either the sample or the excitation spot. Typically the point-scanning approach is employed in confocal microscopy, in which focusing the excitation into a single point allows the

subsequent rejection of out-of-focus fluorescence, by placing a small pinhole onto the detection path, at a conjugate image plane with respect to the microscope's focal plane (*Chapter 2.1.4.*).

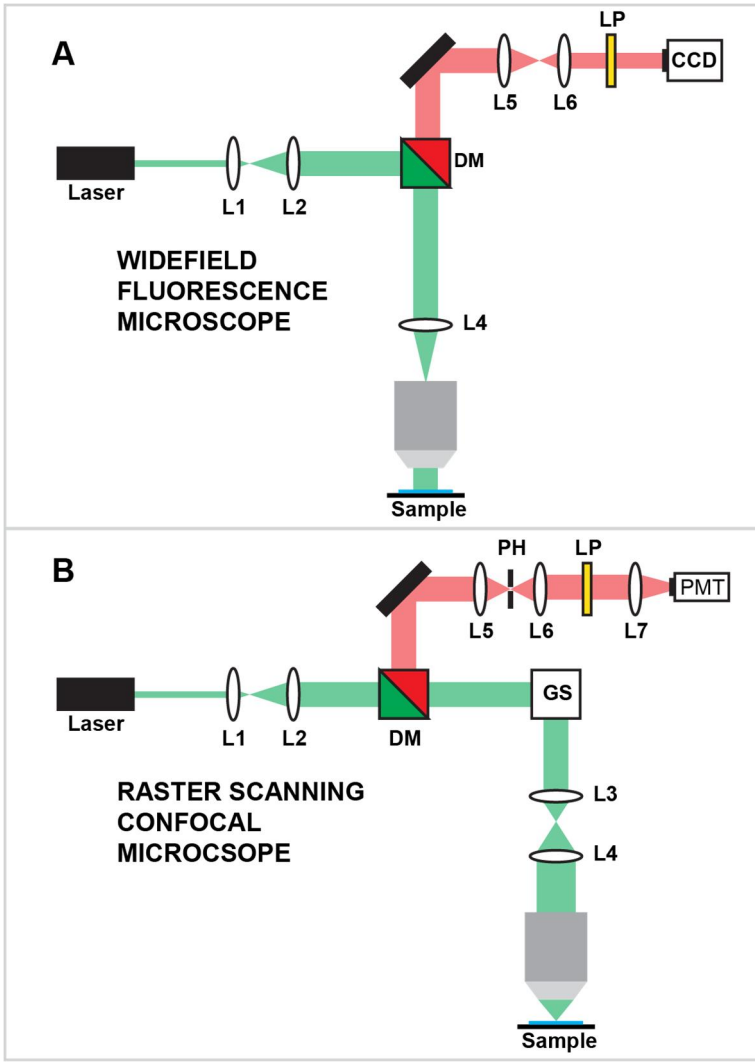

*Figure 1: Example optical setups for a wide-field fluorescence microscope **A** and a raster-scanning confocal microscope **B** are shown. In **A** the excitation light is focused to the back aperture of the objective in order to illuminate the entire FOV. The entire image is acquired at once with a camera. In **B** the excitation light is focused into a single diffraction limited spot, after which the fluorescence signal is measured with a PMT. The raster-scanning in **B** is realized with a galvanometric scanner (GS), coupled with the lenses L3 and L4. A pinhole is used in **B** to reject out-of-focus light. The telescope lens pairs (e.g. L1-L2) are used in both systems to adjust the diameter of the excitation or emission light beams to suit the size of the microscope optics. A dichroic mirror (DM) and a long-pass (LP) filter are used to separate the excitation light from the fluorescence emission signal.*

2.1.2. Resolution and contrast

The classical, and most common definition for resolution is defined as the smallest distance where two point sources can be observed as two separate objects, when viewed through the microscope system. The lateral resolution limit of a fluorescence microscope can be estimated from the Rayleigh criterion to be:

$$d_{xy} = 0.61\frac{\lambda}{n\sin\alpha} \qquad \text{(Eq. 2.1.)}$$

, where λ is the wavelength of light and $n\sin\alpha$ is the numerical aperture (NA) of the objective. The numerical aperture is defined as the product of the refractive index of the immersion medium and the sine of the objective's focusing aperture half angle. The maximum aperture half angle in a single objective is limited to below ~90°, which limits the NA to below ~1.5, when using oil immersion. Therefore the theoretical maximum lateral resolution in an optical microscope is limited to approximately one-third of the wavelength of light, although in practice it is commonplace to talk about one-half of the wavelength of light as the limit.

The resolution equation in the axial direction can be written as:

$$d_z = \frac{2\lambda\eta}{\left(n\sin\alpha\right)^2} \qquad \text{(Eq. 2.2.)}$$

, where η is the refractive index of the object mounting medium. The axial resolution is strongly dependent on the numerical aperture of the objective. It is also evident from *Equations 2.1* and *2.2* that the lateral and axial resolutions do not match ($d_z/d_{xy} = 3.28\,\eta/\mathrm{NA}$), but instead lateral resolution is approximately three times superior even with the highest numerical aperture lenses, with the ratio worsening as the NA is reduced (Inoué 1990).

The definition of the image resolution assumes that there is enough contrast to distinguish two point sources, if they are separated by distance

equal or larger than the conditions expressed in *Equations 2.1* and *2.2*. This however holds true only in theory. In practice the usability of microscope images depends on the signal-to-noise ratio $SNR = signal/\sqrt{signal}$ and the amount of out-of-focus background signal. Confocal microscopes for example have a good background rejection capability, but they suffer from low signal collection efficiency; with wide-field microscopes on the other hand typically good signal level can be recorded, but especially with thick samples the out-of-focus fluorescence seriously degrades the image contrast (Murray *et al.* 2007). Different factors affecting the SNR and contrast in fluorescence microscopy are reviewed in (Waters 2009). Pixelation is a result of sampling of the fluorescence intensity at discrete spatial positions, and in case of undersampling below the Nyquist limit, it also limits the usable details (resolution) in a microscope system (*Chapter 2.1.3.*).

2.1.3. Sampling

Fluorescence microscopy images are produced, by sampling the fluorescence signal intensity at discrete grid positions. The sampling should ideally be adjusted to allow the recording of images at the full spatial resolution (*Chapter 2.1.2.*). According to the Nyquist theorem this can be achieved by adjusting the image pixel size to $1/2\sqrt{2}$ of the expected optical resolution, when using a rectangular sampling grid. Undersampling, i.e. the use of a pixel size larger than stated by the Nyquist criterion, will result into loss of detail and aliasing effects, but the images may still be useful for obtaining information of the full FOV, if the limitations are taken into account – quantitative structural information however, is lost. In many live-cell imaging applications the higher dynamic range allowed by the larger pixels is more important than the maximum resolution, and thus undersampling is used (Waters 2007). Also while oversampling does not improve resolution, in some instances it is used to allow more precise localization of single fluorescent molecules, as the

SNR for the localization is increased (Churchman *et al.* 2005; Yildiz & Selvin 2005; Betzig *et al.* 2006; Rust, Bates & Zhuang 2006; Manley *et al.* 2008)

In wide-field microscopes the pixel size can be adjusted by the magnification, which defines how many times larger the observed image is than the original object. Magnification is not a measure of resolution, but is in practice closely related to it – as choosing the correct magnification, allows the tuning of the pixel size in the recording instrument to match the maximum optical resolution. For example, a quite typical microscope camera has a pixel size of 13x13µm. If such a camera is used together with 100x magnification optics, the maximum observable resolution is 0.37µm, if Nyquist sampling on a rectangular grid is followed, as discussed above. This kind of configuration would match optical resolution achievable with an objective of NA 1.0 at 590nm. It should be noted that the total magnification of a microscope does not necessarily match the magnification of the objective, as it also depends on the intermediate optics between the objective and the camera.

In a raster-scanning microscope the issue of the pixel size is more straightforward to address, as it can be changed by simply adjusting the number of pixels/line or the scan area dimensions; the same amount of pixels in a smaller area make for a smaller effective pixel size, and vice versa. Once the pixel size is set to the theoretical limit, there is no use to decrease it further – increasing magnification will not increase resolution. It should also be noted that magnification as a term is often misused: it is not uncommon to find e.g. presentations from less experienced microscopists, where the presenter states the magnification of their images projected on a wall – a scale bar with the true physical dimensions of the sample should always be used instead.

2.1.4. Optical sectioning

In order to improve contrast when imaging thick biological samples, confocal microscopy technique was developed (Minsky 1961, 1988; Aslund *et al.* 1983; Carlsson & Åslund 1987). Instead of illuminating the whole sample at once, the fluorescence excitation is focused on a single spot, after which only the in-focus (focal plane) part of the emitted light is collected, by using a "volumetric filter": a pinhole that is placed in front of the fluorescence detector, at a conjugate plane with respect to the microscope's focal plane. The pinhole diameter should be ideally adjusted such that the fluorescent volume containing 60-80% of a single Airy pattern is allowed to pass (Conchello, Kim & Hansen 1994; Sandison *et al.* 1995). In theory the use of a pinhole allows a modest, factor of $\sqrt{2}$ increase in both lateral and axial resolution, compared to wide-field techniques – in practice this kind of improvement can rarely be benefited from due to the limited SNR in confocal microscopy images (*Chapter 2.1.2)*. In fact, the most significant advantage in using a confocal microscope is its particular ability to significantly increase contrast, especially with thick and scattering specimen, by limiting the detected fluorescence emission to a thin slice within the sample, thus enabling optical sectioning (Wilson & Carlini 1988; Sandison *et al.* 1995; Murray *et al.* 2007; Wilson 2011).

There are a number of other ways to achieve optical sectioning, in addition to confocal microscopy. Lightsheet microscopy (Voie, Burns & Spelman 1993; Huisken *et al.* 2004; Chen *et al.* 2014) achieves optical sectioning by illuminating an axial section of the sample with a thin sheet of light, that is orthogonal to the detection optical axis – this allows recording of the whole FOV at once with a camera, similarly to wide-field techniques, while still maintaining the confocal-like optical sectioning capability. In two-photon microscopy (Denk, Strickler & Webb 1990; Hänninen, Soini & Hell 1994), the excitation of fluorophores requires the absorption of two photons

within a time period of ~10^{-18}s – the quadratic dependence of the fluorescence excitation from the illumination intensity intrinsically limits the fluorescence within the focal volume of the microscope objective, and thus no pinhole is required for optical sectioning (Benninger & Piston 2013). A further advantage of multi-photon microscopy is its relatively low phototoxicity, due to low infrared light absorption in biological tissue. Multi-photon microscopy can be used to image deep biological scattering tissue, up to one millimeter (Theer, Hasan & Denk 2003).

Several approaches to reduce out-of-focus background in wide-field techniques have been proposed as well. In total internal reflection fluorescence (TIRF) microscopy (Ambrose 1956; Axelrod 1981) only a very thin section at the cover glass surface is illuminated by taking advantage of the total internal reflection phenomenon that is due to lower refractive index of the sample solution, compared to the microscope glass. Recently structured illumination based techniques have been proposed to improve optical sectioning (Neil, Juskaitis & Wilson 1997; Neil, Juškaitis & Wilson 1998; Gustafsson 1999), as well as optical resolution (*Chapter 2.3.*). There are also a number of post-processing methods, based on image deconvolution, that have been proposed to improve optical sectioning capabilities of the wide-field techniques (*Chapter 2.1.5.*). However, in the optical transfer function (OTF) of a wide-field microscope the frequency area that is required for axial sectioning is missing, which limits the usefulness of the post-processing approaches, unless optical information is collected to compensate for the missing information – e.g. by dense sampling in the axial direction or by structured illumination (Agard *et al.* 1989; Gustafsson, Agard & Sedat 1995).

2.1.5. Deconvolution

In most image processing tasks at least some form of contrast enhancement is used. In its simplest form, this may entail the stretching of the image his-

togram to the full dynamic range or enhancing the edge contrast with unsharp masking. Moving beyond these simple day-to-day operations, by e.g. image deconvolution it is possible to significantly reduce the out-of-focus blur as well as random noise and other aberrations. Deconvolution mathematically reconstructs the original object from the image data, with the presumption that the point spread function (PSF) of the microscope system is known or can be estimated from the images. This enables optical sectioning in wide-field microscope systems without an optical pinhole – such mathematical sectioning naturally requires at least some contrast between in-focus and out-of-focus details and can be improved by increasing the SNR of the images by dense depth sampling (Shaw 2006). In confocal-based microscopes much of the out-of-focus light is blocked by the pinhole but even with those images, deconvolution can still significantly increase image contrast and apparent resolution (Shaw 2006).

Image formation in a microscope can be described as a convolution of every object sample point with the microscope's PSF:

$$i(x,y,z) = h(x,y,z) \otimes o(x,y,z) \;\; || \;\; x,y,z \in D \qquad \text{(Eq. 2.3.)}$$

, where *i(x,y,z), h(x,y,z)* and *o(x,y,z)* are the measured image, the microscope's PSF and the original sample object, respectively. *D* is the set of pixel positions in the image and $\otimes$ denotes convolution. The convolution operation becomes a regular pixel-wise multiplication operation in frequency domain, and thus the most intuitive way for performing deconvolution is just inverting the convolution process by division:

$$O(f_x,f_y,f_z) = \frac{I(f_x,f_y,f_z)}{H(f_x,f_y,f_z)} \;\; || \;\; f_x,f_y,f_z \in F \qquad \text{(Eq. 2.4.)}$$

, where $I(f_x, f_y, f_z)$, $H(f_x, f_y, f_z)$ and $O(f_x, f_y, f_z)$ are the frequency domain representations of the measured image, PSF and the original object. *F* is the set of spatial frequencies in the images. In practice such an approach is not without

difficulties, as the near-zero values in the PSF at high frequencies lead into strong amplification of noise – also the finite image size in this direct deconvolution will create artifacts as a consequence of the assumption of continuous signals. In Wiener-filter based deconvolution algorithms (as in *Equation 2.4*), the problem is addressed by adding a non-zero value to the denominator, or by setting pixel values where $H(f_x, f_y, f_z)$ is small to zero; such approaches do attenuate the noise, but at the same time fine detail in the image is blurred (Shaw 1994; McNally *et al.* 1999; Cannell, McMorland & Soeller 2006). Alternatively deconvolution can be seen as a minimization problem:

$$\min \left\| h(x,y,z) \otimes o(x,y,z) - i(x,y,z) \right\|^2 \qquad \text{(Eq. 2.5.)}$$

, which is the basis of linear-least-squares (Preza *et al.* 1992) and Tikhonov filtering approaches (Tikhonov & Arsenin 1977). The difference between the reconstructed original sample object convolved with the system PSF, and the measured image is mostly due to noise, which is assumed Gaussian in both least squares and inverse filtering methods. Both inverse filtering and least-squares algorithms, are computationally simple, but they only lead to modest image quality improvement, and they are also very sensitive to noise and errors in the PSF (Cannell *et al.* 2006; Sarder & Nehorai 2006).

Today, in most practical applications some form of an iterative deconvolution algorithm is utilized (Jansson, Hunt & Plyler 1970; Carrington 1990; Van Der Voort & Strasters 1995; Sarder & Nehorai 2006), as they produce much improved image quality, especially with noisy data. Richardson-Lucy (Richardson 1972; Lucy 1974) iterative algorithm, which has been found especially suitable for deconvolution of noisy images, implements deconvolution as a statistical maximum-likelihood (ML) estimation task:

$$o_{k+1} = \left\{ \frac{i}{h \otimes o_k} \otimes h^* \right\} o_k \qquad \text{(Eq. 2.6.)}$$

, where o_k and o_{k+1} are the current and the next estimates for the original ob-

ject, h is the PSF and h^* its mirrored version and i is the original image; in the equation, the pixel indexes have been omitted to allow a simpler presentation of the algorithm. The Richardson-Lucy deconvolution in *Equation 2.6* assumes the presence of Poisson noise, which is the correct model for the photon counting shot noise in fluorescence microscope images (Sheppard *et al.* 2006). However, based on comparisons of different deconvolution methods in (Verveer, Gemkow & Jovin 1999), the selection of a noise model does not seem to be very critical to the deconvolution results. A mathematically simpler version of *Equation 2.6* can be written, when noise is assumed to be Gaussian (Cannell *et al.* 2006):

$$o_{k+1} = o_k + (i - o_k \otimes h) \otimes h^* \qquad \text{(Eq. 2.7.)}$$

The Richardson-Lucy algorithm tends to amplify noise, because when the deconvolution process approaches convergence, the algorithm also tries to fit the noise in the measured image to the ML estimate. One way to deal with this issue, is to blur the measured image before deconvolution, or to manually stop the deconvolution process at some intermediate step, before complete convergence (Carrington 1990; McNally *et al.* 1999). Alternatively various regularization methods have been proposed (Van Kempen & Van Vliet 2000; Dey *et al.* 2006; Laasmaa, Vendelin & Peterson 2011) to deal with the noise amplification.

In the deconvolution methods discussed above, it is assumed that the PSF of the microscope system is known. This requirement can be relaxed by utilizing blind deconvolution methods, in which the PSF is estimated from the measured images (Holmes, Biggs & Abu-Tarif 2006). This can be achieved for example with the Richardson-Lucy method, by simultaneously finding estimates for the original image and the system PSF (Holmes 1992; Fish *et al.* 1995; Krishnamurthi *et al.* 1995).

2.2. Super-resolution microscopy

The Rayleigh criterion (*Chapter 2.1.2*) states that the lateral resolution in any optical microscope is limited by diffraction to at best one third of the wavelength of light, whereas the axial resolution is three times inferior or worse, thus comparable at best to the wavelength of light. The term super-resolution, as is intended here, generally describes both methods to improve the lateral and/or the axial resolution of the microscope beyond the diffraction limit, and methods to optimize the light collection capability of the microscope, in order to achieve the theoretical diffraction-limited maximum resolution. The diffraction limit still holds true in super-resolution microscopy methods as well: it is not possible to focus light beyond it in far-field microscopy, but several methods have been introduced to circumvent it.

2.2.1. Lateral super-resolution

In (Hell & Wichmann 1994) a method to surpass the diffraction limit in a point-scanning confocal microscope system was proposed. It was speculated that it should be possible to switch-off fluorescent molecules within a diffraction limited confocal excitation spot, by taking advantage of the stimulated emission phenomenon. The ability of stimulated emission to switch-off fluorescent molecules was experimentally demonstrated in (Hell *et al.* 1995), and later on, a super-resolution stimulated emission depletion (STED) microscope based on this principle was introduced (Klar & Hell 1999; Klar *et al.* 2000). STED uses point illumination to excite all fluorophores inside a diffraction limited focal spot, but immediately after the fluorescence excitation, most of the fluorophores are switched off by applying a depletion laser beam at a wavelength red-shifted from the fluorophore's emission peak. In order to not to switch-off all the fluorescence in the excitation volume, a phase-modified depletion beam with a zero intensity center is used. Fluorescence is only allowed within the zero-intensity center of the focal spot, and thus the optical resolution depends on its size, which decreases with increas-

ing depletion intensity, thus enabling theoretically unlimited resolution. An image is formed just like in a confocal microscope, by raster-scanning the FOV point-by-point. The raster-scan step size naturally needs to be small enough to allow sufficient sampling for the increased optical resolution (*Chapter 2.1.3*). The original STED system (Klar *et al.* 2000) was implemented with pulsed excitation, because synchronization of excitation and depletion are conveniently done in pulsed mode, and with pulsing the high illumination intensity required for efficient fluorescence depletion is easy to achieve. More recently continuous depletion has been enabled as well (Willig *et al.* 2007). The resolution in STED can be further increased by utilizing pulsed excitation with gated detection that discards photons that are detected earlier than indicated by the fluorescence lifetime (Vicidomini *et al.* 2011); the early photons originate from the fluorescence depletion process. Also post-processing (deconvolution) methods have been proposed to further increase the SNR and apparent resolution, with moderate depletion intensities (Castello, Diaspro & Vicidomini 2014). The saturable on/off switching mechanism utilized in STED can be realized in several other ways in addition to stimulated emission depletion, for example (Hell & Kroug 1995; Hofmann *et al.* 2005; Bretschneider, Eggeling & Hell 2007; Grotjohann *et al.* 2011) – these (including STED) are commonly called Reversible Saturable Optical Fluorescence Transitions (RESOLFT) techniques (Hell, Jakobs & Kastrup 2003; Hell 2004).

In (Betzig 1995) it was speculated that it should be possible to resolve multiple features within a single diffraction limited spot, by first isolating each individual feature and then calculating their precise spatial coordinates. While it is not possible to resolve multiple details within a single diffraction limited volume, it is possible to calculate the center position of the spot to a nearly arbitrary precision (Gelles, Schnapp & Sheetz 1988; Thompson, Larson & Webb 2002; Yildiz & Selvin 2005), as long as sufficient number of photons are recorded, at an appropriately precise sampling rate (*Chap-*

ter 2.1.3). In (Betzig *et al.* 2006; Rust *et al.* 2006; Hess, Girirajan & Mason 2006) super-resolution wide-field microscopy methods, PALM, STORM and FPALM were introduced, based on this concept. They take advantage of the property of certain fluorescence molecules to be selectively (stochastically) switched on or off, by applying excitation light at a particular wavelength. While the various implementations differ slightly, the principle of achieving the super-resolution is the same:

1. A small subset of the fluorophores in the FOV is enabled stochastically by applying a low-intensity photo-activation pulse, the intensity of which should be such that the probability of enabling more than one fluorophore inside a diffraction limited spot or its vicinity is diminishing.
2. The enabled fluorophores are excited and imaged, after which they are either bleached (Betzig *et al.* 2006; Hess *et al.* 2006) or switched off (Rust *et al.* 2006).
3. The precise spatial coordinates for each of the fluorophores in the image are calculated.
4. The imaging and localization cycle is repeated from 10^4 to $>10^5$ times (Betzig *et al.* 2006), and the localization results are accumulated to form a complete localization image.

More recently methods have been introduced that enable localization-based super-resolution with standard fluorophores (Heilemann *et al.* 2008; Folling *et al.* 2008; Baddeley *et al.* 2009).

In structured illumination microscopy (SIM) (Gustafsson 1999), instead of relying on specific optical properties of fluorophores, resolution increase is achieved by illuminating the sample in a regular wide-field microscope with a spatial pattern, which can consist of dark and light stripes, or a more complex shape. The shape can even be unknown (Mudry *et al.* 2012). The illumination pattern modulates the high-frequency details in the sample,

making them visible in a regular diffraction limited image as low frequency moiré fringes – afterwards the fine details can be extracted and moved back to their right frequency spectral place with image reconstruction. Depending on the shape of the illumination pattern, several images with different pattern orientations may be required to achieve resolution increase in two dimensions. The resolution improvement of the regular SIM is limited to the factor of two, because the smallest possible size of the pattern is also limited by diffraction. In (Gustafsson 2005) a theoretically unlimited resolution was demonstrated in SIM with a nanoparticle sample, by taking advantage of the non-linear response of fluorescence molecules to increased excitation intensity, after fluorescence saturation has been reached. In (Rego *et al.* 2012; Li *et al.* 2015) ~50 nm resolution in biological samples was demonstrated with the non-linear SIM.

2.2.2. Axial super-resolution

The fluorescence emission from a microscope's focal spot can be assumed to occur in all directions, and thus for maximum resolution light should be collected 360° around the sample. In a single objective microscope however, the maximum theoretical aperture is 180° – in practice a bit less due to mechanical limitations. Therefore, a significant amount of information is missing, especially in the axial direction, which leads to the anisotropic optical resolution in lateral and axial directions in all single objective microscope systems, as discussed in *Chapter 2.1.1*. Therefore, the most obvious way to improve the axial resolution in a microscope is to increase the light collection capability of the system, by placing a second objective behind the sample. In order to take advantage of the second objective however, the sample either needs to be illuminated coherently through the two objectives, or the images from the two objectives need to be coherently coupled into a single detector – or one can also do both simultaneously. Coherent illumination results into constructive interference at the focal spot, and destructive interference at ap-

proximately λ/4 distance from the focus. Similarly, coupling the images from both of the objectives to a single detector, in a way that the optical path lengths are equal, results into constructive interference at the image. Employing both of the methods in a single instrument enhances both the excitation and the emission PSFs, and thus the product of the two, the effective PSF of the system is further enhanced. Interferometric coupling of two beams leads to constructive interference also outside the main optical focus, causing the creation of side-lobes that need to be removed by image processing after image acquisition (Hell & Stelzer 1992; Gustafsson *et al.* 1995; Hänninen *et al.* 1995).

In 4Pi microscopy techniques two opposing objectives are coherently used in laser scanning confocal microscopy. There are three types of 4Pi microscopes: type A for coherent illumination, type B for coherent detection and type C for combined coherent illumination and detection (Hell & Stelzer 1992). Type C provides the highest <100nm resolution (Hell *et al.* 1994), but it is also the most complex of the methods, as both the illumination and detection paths need to be matched. The STED super-resolution technique has also been coupled with a 4Pi microscope, to produce a super-resolution microscope with isotropic ~50 nm resolution (Schmidt *et al.* 2008). It is also possible to improve the axial resolution in a single objective STED by introducing an annular depletion shape for the axial direction (Klar *et al.* 2000; Wildanger *et al.* 2009); however the annular depletion shape deteriorates quickly in scattering media (Deng *et al.* 2009), limiting the practical super-resolution optical sectioning capabilities of such systems. Recently an adaptive optics based approach was proposed to mitigate this problem (Gould *et al.* 2012).

I^5M implements a technique similar to 4Pi type C on a wide-field fluorescence microscope (Gustafsson *et al.* 1995; Gustafsson, Agard & Sedat 1999). The sample is illuminated through two opposing objectives with in-

coherent light, in order to produce a patterned illumination profile that modulates the axial fine detail within the focal volume – the details can be later recovered by reconstruction, similarly to what is done in SIM (*Chapter 2.2.2*). As in 4Pi type C, images from both of the objectives are coupled into a single detector, in order to produce interference at the common focus. Axial resolution of approximately 70-90 nm with biological samples was demonstrated in (Gustafsson *et al.* 1995, 1999), however, the axially repeating interference pattern limits the applicability of the technique in depth and with denser samples (Bewersdorf, Schmidt & Hell 2006). In iPALM (Shtengel *et al.* 2009), a modified PALM super-resolution microscope, two opposing objectives were used in a wide-field configuration to obtain <10 nm resolution in all three dimensions – the axial detail was resolved by simultaneous multiphase interferometry; the detection side-lobes together with the employed near-TIRF illumination limit the applicability of the iPALM technique to very thin samples. It is also possible to improve axial resolution in single objective wide-field systems. The structured illumination technique (*Chapter 2.2.1.*) can be used to double axial resolution in a single objective system, by introducing an illumination pattern for the axial direction (Gustafsson *et al.* 2008). The same principle was recently taken advantage of in a lattice lightsheet system to enable fast super-resolution imaging (Chen *et al.* 2014). In (Huang *et al.* 2008) a cylindrical lens was inserted in a STORM localization microscope to produce an optical astigmatism, which allowed localization in the axial direction at sub-100nm resolution. In (Juette *et al.* 2008) similar resolution was reported in a FPALM localization microscope system, modified to simultaneously record two axial planes.

In Theta microscopy (Stelzer & Lindek 1994) two separate objectives are used for illumination and detection, such that the detection objective is in orthogonal orientation in relation to the illumination objective. This in principle allows taking advantage of the superior lateral resolution, to resolve axial detail. While conceptually interesting, such configuration requires the

use of low NA objectives, and thus the practical resolution gain in Theta microscopy, when compared to regular single objective systems with high NA optics, is limited (Sätzler & Eils 1997; Gustafsson 1999). Axial tomographic methods on the other hand, discussed in *Chapter 2.3*, take full advantage of the same concept to improve axial resolution in standard single objective microscopes.

2.3. Tomographic super-resolution microscopy

In *Chapter 2.2.2* different physics-based solutions were discussed for addressing the anisotropic resolution issue in optical microscopes. With axial tomographic methods similar results can be obtained, by taking advantage of mathematical image reconstruction algorithms, often similar to image deconvolution methods overviewed in *Chapter 2.1.5*. The benefit of tomographic methods is that they are applicable to any type of a microscope system. One only needs to establish a method to acquire the necessary projections.

2.3.1. About axial tomography

Axial tomographic methods can be employed when one desires to use the superior lateral resolution in optical microscopes to resolve axial detail. This can be achieved by acquiring several views (projections) of the sample at different observation angles, after which the views are combined into a single image (tomogram), which contains the highest resolution information from each of the view directions. Observing the sample from multiple angles increases thus the effective numerical aperture of the microscope system, similarly to the multiple-objective methods discussed in *Chapter 2.2.3*, although in tomographic methods the improvement of the effective NA bases on mathematical multi-image reconstruction, rather than the physical increase of the NA. According to mathematical simulations in (Sätzler & Eils 1997) a tomogram with nearly isotropic resolution can be reconstructed from

four or more views with identical angular spacing in axial tomographic fluorescence microscopy. A further benefit of axial tomographic methods is that they enable the imaging of opaque or very thick samples, even beyond the working distance of the microscope objective, because the complete image can be reconstructed from the partial projections (Huisken *et al.* 2006; Swoger *et al.* 2007; Krzic 2009). Axial tomographic methods have been taken advantage of in wide-field microscopy (Shaw *et al.* 1989; Shaw 1990; Bradl *et al.* 1992; Cogswell, Larkin & Klemm 1996), lightsheet microscopy (Huisken *et al.* 2004; Verveer *et al.* 2007; Swoger *et al.* 2007; Krzic 2009; Temerinac-Ott *et al.* 2012), confocal microscopy (Heintzmann & Cremer 2002; Renaud *et al.* 2008; Remmele *et al.* 2011) and localization super-resolution microscopy (Tang *et al.* 2010).

Typically the different views are acquired by tilting the sample around an axis orthogonal to the main optical axis, after which the sample is moved through the optical focus to acquire a 3D stack. To forgo the physical rotation, methods for simultaneous detection of multiple views have been proposed (Swoger, Huisken & Stelzer 2003; Krzic *et al.* 2012; Tomer *et al.* 2012). In (Laksameethanasan *et al.* 2008; Saux *et al.* 2009; Yu *et al.* 2011) only a single image was acquired for each observation angle, rather than a 3D stack – a 3D tomogram was reconstructed from the rotated 2D projections, similarly to what is done for instance, in computed X-ray tomography. In (Punge *et al.* 2008; Nanguneri *et al.* 2012) mechanical sectioning of the sample was used to provide a series of sub-resolution slices, from which a higher resolution tomogram could be reconstructed; in such techniques the axial resolution is determined by the sample thickness, rather than the optical resolution.

2.3.2. Tomographic reconstruction

Axial tomographic reconstruction consists of two tasks: image registration and image fusion. The image registration involves the transformation of the

different views into a common coordinate system, followed by the fine alignment of the image details. The image fusion combines the best information from the single views into a single high quality tomogram.

The purpose of the image registration is to find a spatial transformation that aligns two views: a *moving image* and a fixed *reference image*. In some cases the registration problem may be approached manually (Heintzmann, Kreth & Cremer 2000), but in most practical applications automatic image registration methods are employed. Algorithmically such a task requires iterative adjustment of the spatial transformation parameters, in order to maximize a similarity measure that has been selected to quantify the degree of alignment of the two views. In (Heintzmann & Cremer 2002) the cross-correlation between two views was used as a similarity measure for rotational alignment, whereas the translational offset was corrected according to the center-of-mass of the cross-correlation function. In (Cogswell *et al.* 1996; Swoger *et al.* 2007) purely translational registration methods, based on cross-correlation were proposed – the different views were rotated into a single coordinate system before the automatic registration, by rotation angles estimated from the instrument settings. In (Remmele *et al.* 2011) registration of confocal axial tomography images was based on minimization of a mean squared difference function. Both the cross-correlation and the mean squared difference functions, by default, use the complete images to calculate the similarity measure. Such approaches become computationally complex with large images. To address this problem in (Preibisch *et al.* 2010) a registration approach was suggested for multi-view lightsheet microscopy images that uses fluorescent nanobeads as fiduciary markers for image alignment. Because the beads are only present in a small subset of image positions, using them as registration landmarks instead of the complete images significantly reduces the computational requirements for the image registration. A further advantage of the beads based registration is that it lends itself well to the use of deformable spatial transformations, as possible deformations are relatively

easy to point out from the offset of corresponding landmarks (Preibisch *et al.* 2010; Temerinac-Ott *et al.* 2012). Disadvantages of such approaches are that special sample preparation is required to add and immobilize the beads – and extra image-processing steps are required to find, utilize and in the end, to remove the beads from the final image.

Once all the views have been registered, they are fused into a single tomogram. In its simplest form a tomogram can be calculated as the pixel-by-pixel arithmetic mean of all the views. This kind of fusion approach was employed in (Cogswell *et al.* 1996; Swoger *et al.* 2007); a slightly more sophisticated weighted blending scheme was proposed in (Preibisch, Saalfeld & Tomancak 2009; Preibisch *et al.* 2010). An alternative approach is to calculate the fusion in the frequency domain, by averaging (Swoger *et al.* 2007) or by selecting the highest amplitudes in the different projections (Shaw *et al.* 1989; Sätzler & Eils 1997) . The latter method was shown to provide superior results to basic averaging in (Sätzler & Eils 1997), however it was also found very sensitive to noise and alignment errors. These simple reconstruction techniques are able to produce tomograms with increased apparent axial resolution, but they do not specifically deal with the axial haze caused by the anisotropic resolution in the individual projections – therefore, the created tomograms are somewhat blurry, as pointed out in (Swoger *et al.* 2007). A more sophisticated reconstruction method, as already indicated in (Shaw *et al.* 1989; Sätzler & Eils 1997), can be created by modifying an iterative deconvolution algorithm (*Chapter 2.1.5*). For example the Richardson-Lucy iterative deconvolution algorithm in equation (*Equation 2.6.* in *Chapter 2.1.5*) can be written to multiple projections:

$$o_{k+1} = \frac{o_k}{N} \sum_{v \in V} \frac{i_v}{o_k \otimes h_v} \otimes h_v^* \qquad \text{(Eq. 2.8.)}$$

, where o_k and o_{k+1} are the current and next fusion estimates, i_v is the v^{th} view in the set of projections V, N is the number of projections and h_v is the PSF

corresponding to the current view, whereas h_v* is its mirrored version. The algorithm in *Equation 2.8* was implemented for axial tomographic images in (Remmele *et al.* 2011; Temerinac-Ott *et al.* 2012). In (Preibisch *et al.* 2014) a multiplicative version of *Equation 2.8* was introduced for fusing multi-view lightsheet microscopy data. The maximum-likelihood algorithm in (Holmes & Liu 1991) was modified to fuse confocal axial tomography images in (Heintzmann *et al.* 2000). Iterative Wiener filtering and maximum a posteriori deconvolution algorithms were implemented in (Swoger *et al.* 2007). Recently a nearly real-time, GPU accelerated iterative fusion method was introduced for multi-view lightsheet images (Schmid & Huisken 2015).

2.4. Super-resolution correlative microscopy

Correlative microscopy methods enable the combination of several imaging modalities, to provide unique information of the problem at hand that could not be obtained with any of the individual techniques alone. The discussion in this chapter is focused on techniques involving super-resolution optical microscopy techniques correlated with electron microscopy or atomic force microscopy techniques. Other correlative imaging modalities are reviewed for example in (Caplan *et al.* 2011).

2.4.1. Correlative super-resolution microscopy methods

Light microscopes (LM) are invaluable tools in biology research, as they allow the tagging of specific structures within cells with fluorescence markers, and optical sectioning allows the observation of these structures in 3D, even within living cells. Electron microscopy (EM) techniques on the other hand provide superior resolution, but they do not allow the observation of living specimen, and tagging specific structures is difficult. A significant amount of work thus has been done to establish correlative light and electron microscopy (CLEM) methods (de Boer, Hoogenboom & Giepmans 2015). Super-resolution microscopy modalities are especially interesting for CLEM

applications, because they allow the fluorescence imaging at the same resolution scale with EM (Watanabe *et al.* 2011; Kopek *et al.* 2012; Chang *et al.* 2014; Löschberger *et al.* 2014; Johnson *et al.* 2015; Kim *et al.* 2015; Wojcik *et al.* 2015).

Atomic force microscopes (AFMs) can provide unique biophysical information of sample surfaces (topology, stiffness etc.), at Ångström-scale resolution. AFMs however lack the bio-specificity of fluorescence labeling, although it is possible to coat the AFM tip with a specific ligand, in order to localize receptors on cell surface, for example (Girish *et al.* 2009) – and the AFM imaging is typically limited to surfaces, although there are exceptions, such as (Osada *et al.* 2003). Optical microscopes on the other hand provide 3D imaging capabilities and enable the use of specific fluorescence labeling, but they cannot provide information on nanomechanical properties of a cell as an AFM does – this makes a correlative LM-AFM approach very attractive. The combination of AFM with super-resolution microscopy techniques is particularly attractive, as they enable optical imaging at similar resolution with AFM (Chacko, Zanacchi & Diaspro 2013b; Monserrate, Casado & Flors 2014; Odermatt *et al.* 2015). It should also be noted, that instead of just correlating images, it is also possible to use the AFM cantilever as a small manipulator, which creates interesting possibilities for correlative microscopy (Chacko *et al.* 2013a, 2014).

2.4.2. Correlating multimodal images

In order to take advantage of correlative imaging, methods to combine the data from multiple imaging modalities need to be established. There are two basic requirements:

1. A common region-of-interest (ROI) needs to be identified in all the modalities.
2. Image alignment needs to be successful e.g. via fiduciary markers that are visible in all modalities.

In CLEM, the imaging is typically done with two separate instruments, although electron microscopes with integrated fluorescence imaging capabilities have been proposed as well. The common ROI can be found in two separate instruments, by way of using a finder grid, for example (Spiegelhalter, Laporte & Schwab 2014). For the image alignment, some kind of fiduciary markers are typically added to the sample to be used as registration landmarks, such as nanoparticles (Kopek *et al.* 2012), quantum dots (Masich *et al.* 2006) or polymer beads (Kukulski *et al.* 2012). In super-resolution CLEM methods image alignment in literature is either done manually in Photoshop (Watanabe *et al.* 2011; Chang *et al.* 2014; Kim *et al.* 2015), or then semi-automatically, by calculating the spatial transformation from manually selected corresponding landmark pairs in ImageJ or Matlab (Kopek *et al.* 2012; Löschberger *et al.* 2014; Johnson *et al.* 2015; Kim *et al.* 2015; Wojcik *et al.* 2015).

For super-resolution LM-AFM correlative imaging it is possible to mount the AFM on the LM system, which makes correlative imaging possible without moving the sample between instruments. The imaging is still separate, and image alignment is required after data-acquisition: in (Odermatt *et al.* 2015) image registration was done automatically by using common image details in LM and AFM images, similarly to methods discussed in *Chapter 2.3.2*, whereas in (Harke *et al.* 2012; Chacko *et al.* 2013b) a proprietary AFM scan field calibration routine was used. Using the AFM as a nanomanipulator in live cell correlative experiments, would require software tools for combined control and synchronization of the two instruments – such tools have not yet been discussed in literature.

2.5. Automated microscope image analysis

Modern microscopy experiments rely strongly on software – computational methods are needed all the way from data acquisition (*Chapter 2.1, 2.2*), data storage, image reconstruction, restoration and alignment (*Chapters 2.1.5,*

2.2, 2.3, 2.4), to quantitative image analysis and image visualization. This chapter concentrates on quantitative image analysis, with special interest in image quality assessment.

2.5.1. About quantitative microscopy

Quantitative automated image analysis is necessitated by the huge amount and complexity of data that modern microscopes produce today – datasets of several terabytes in size can easily be generated (Keller *et al.* 2011; Wang *et al.* 2014; Chen *et al.* 2014). There is also a great interest in live-cell experiments, which involve imaging of the sample over long periods of time – as a result the amount of data grows well beyond the possibilities of subjective (manual) data analysis (Neumann *et al.* 2010; Fernandez *et al.* 2010). Moreover there is a general consensus in scientific community today that biological findings based on microscope images, should be supported by sound statistics, produced by quantitative analysis of those images ("The quest for quantitative microscopy (Editorial)" 2012). Producing such statistics manually is tedious at best even with relatively small amount of images, and impossible when moving into more complex experiments, for example high content microscopy, in which thousands upon thousands of images need to be analyzed. Therefore automatic quantitative image analysis tools are being developed to produce the necessary measures (Ljosa & Carpenter 2009; Shariff *et al.* 2010).

2.5.2. Qualitative quantitative image analysis

Successful quantitative analysis requires the establishment of methods to recognize relevant structures in images. When datasets are relatively small, one could still be tempted to subjectively select the suitable images, and then analyze them one by one with manual image segmentation and analysis tools in BioimageXD (Kankaanpää *et al.* 2012) or Fiji (Schindelin *et al.* 2012) for example. In more complex cases the data analysis software must be taught to

recognize the relevant details in images automatically (Huang & Murphy 2004; Shamir *et al.* 2010). It has been proposed that such objective computer vision based segmentation tools could eventually be relied on to select the representative images even for publications (Markey, Boland & Murphy 1999).

Before attempting any type of an automated quantitative analysis, one must establish a method to exclude certain *outlier* images from analysis, as for example out-of-focus images are quite commonly produced in high-content microscopy experiments, and they corrupt the quantitative measures, if not taken into account (Firestone *et al.* 1991; Brázdilová & Kozubek 2009; Bray *et al.* 2012). On the other hand, if the computer can be trained to discard low quality images, it should also be possible to turn the problem upside down and train it to recognize high quality images. Such automated image quality assessment methods have only been applied to microscopy on a few occasions (Paul *et al.* 2008; Redondo *et al.* 2012; Bray *et al.* 2012).

3. AIMS OF THE STUDY

This thesis covers different aspects of bioimage informatics software, especially developed for STED super-resolution microscopy. The basic aims can be divided as follows:

I. **Development of axial tomographic STED microscopy technique and image reconstruction software**. With such method near isotropic resolution can be achieved with a regular 2D STED system. In addition, tomographic techniques potentially enable relatively fast super-resolution imaging of large specimen in 3D, which is currently out of reach of any STED microscopy technique.

II. **Development of software tools for correlative super-resolution microscopy**. Super-resolution microscopy enables fluorescence imaging at similar resolution-scale with AFM or TEM for example. Correlative imaging potentially enables the combination of the strengths of different microscopy techniques, to provide unique insight into the sample object.

III. **Development of software tools for automatic image quality assessment of super-resolution images.** With the growing size of microscopy image datasets, it is becoming increasingly challenging to find the relevant images for image analysis, and in many image analysis tasks sub-optimal images corrupt the quantitative results, if not dealt with properly. Automatic image quality assessment can help in both of these cases.

4. MATERIALS & METHODS

In this chapter a short summary of the materials and methods employed in the study is given. A detailed description can be found in the original publications (**I**-**IV**). In addition, some previously unpublished materials and methods are presented (Prabhakar *et al.* Unpublished).

4.1. Image acquisition

4.1.1. STED< axial tomography data acquisition

In order to enable axial tomographic reconstruction (*Chapters 4.2.1 & 4.2.2*, **I-II**), several views of the sample must be obtained from different observation angles. As discussed in *Chapter 2.3.1* typically the projections are obtained by rotating the sample. In (**I**) we proposed that a second view of the sample could be obtained through a small mirror that was placed on top of a standard microscope cover glass, at an angle of 20°-30° from the sample plane (*Figure 2*) enabling a second 40°-60° tilted view STED< of the sample, with respect to the regular STED image. In (**I**) an AFM (Agilent 5500ilm, Keysight Technologies, USA) with a gold-coated cantilever tip was used to provide the oblique view of the sample. This allowed the easy maneuverability of the mirror position, but also somewhat complicated the acquisition system. For (**II**) a custom rotation/translation (XYZ) stage assembly was developed.

All the imaging was done with a standard commercial Leica TCS STED microscope (Leica Microsystems, Germany), with an oil immersion objective lens (Leica STED NA 1.4, 100x). The samples were mounted in TDE (liquid) to allow the placement of the mirror in contact with the sample and the tuning of the refractive index to exactly match that of the immersion oil 1.518, which is important in order to minimize optical aberrations, when acquiring an image stack via the mirror. The pixel size was set to 23nm (xy), 250nm (z) to meet the Nyquist criterion. The two images were acquired in

sequence: first the standard STED image and then the STED< image – the sample was not moved, and only axial (z) refocusing was required. The images were acquired normally with the Leica LAS AF (Leica Microsystems, Germany) software and stored for processing in our *SuperTomo* software. The *SuperTomo* image reconstruction method is described in *Chapter 4.2* and a pseudocode description of the software is given in *Chapter 4.5*.

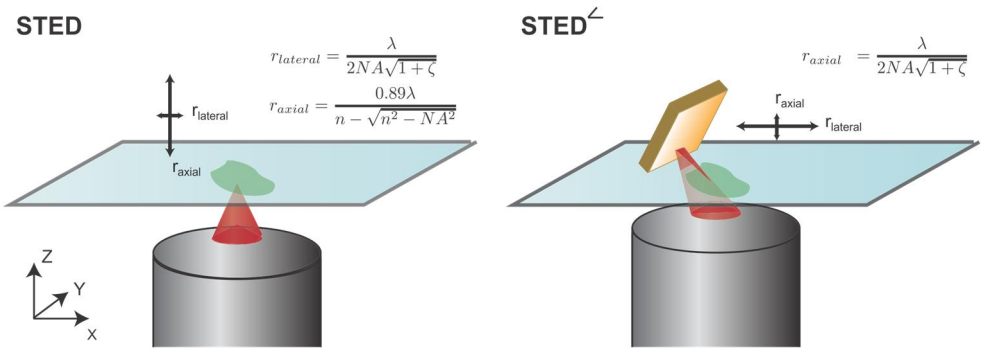

Figure 2: The STED< data acquisition method is illustrated. First a regular STED image is acquired, after which an oblique view of the sample is obtained by refocusing through a small mirror that was placed on top of a standard microscope cover glass, at an angle of 20°-30° from the sample plane. The Figure was reproduced from ***I****.*

4.1.2. STED-AFM correlative setup

In (**III**) a correlative STED-AFM imaging system was developed. The fundamental idea was to create a software framework for correlative STED-AFM studies that enables (1) the synchronized control of data acquisition in two separate arbitrary instruments and (2) the automatic correlation of imaging results. *StedAfmCorr* software was created for these purposes.

A Leica TCS STED microscope (Leica Microsystems, Germany) was used for STED imaging whereas Agilent 5500 ILM (Keysight Technologies (former Agilent), USA) was used for AFM imaging. As a starting point, the two systems were completely incompatible for the selected task without modifications, i.e. there was no existing method for using them for correlative experiments; the AFM could not even be mounted on the STED system.

Therefore, a custom stage was fitted on the STED system. As can be seen in *Figure 3B*, the AFM scans the sample from the top, whereas STED takes super-resolution images from the opposite side. The data acquisition in the two instruments can be done independently, or alternatively in synchronized manner through our developed *StedAfmCorr* software. The data acquisition in the AFM is controlled through a proprietary PicoScript (Keysight Technologies, USA) application programming interface (API). No API is provided for the Leica LAS AF (Leica Microsystems, Germany) software in our STED microscope, but data acquisition workflows can be designed in the Live Data Mode advanced experiments interface, and their progress can be controlled and observed via external hardware trigger signals (*Figure 3A*). The hardware triggers allowed us to control the STED data acquisition in our *StedAfmCorr* software, with the help of a digital I/O card (USB-6501, National instruments, USA).

In order to create fiduciary markers for image correlation, reflection images of the AFM cantilever tip at the corners of the AFM scan area were acquired with the STED instrument in confocal reflection mode. A workflow was created in Leica LAS AF Live Data mode to acquire the desired number of landmark images after each STED image. The *StedAfmCorr* software could then be used to automatically acquire an AFM image, STED image and the necessary landmark images; *StedAfmCorr* also takes care of the automatic positioning of the AFM tip to the corners of the scan area. After data acquisition *StedAfmCorr* can be used further to automatically correlate the images (*Figure 3C*), although due to the lack of an API for Leica LAS AF software, the user needs to manually save the STED images in order to make them available for *StedAfmCorr*. Two image registration methods, automatic and semi-automatic were implemented, as discussed in *Chapter 4.2.1*. A pseudocode descriptions of the implemented image registration and instrument control features are given in *Chapter 4.5*.

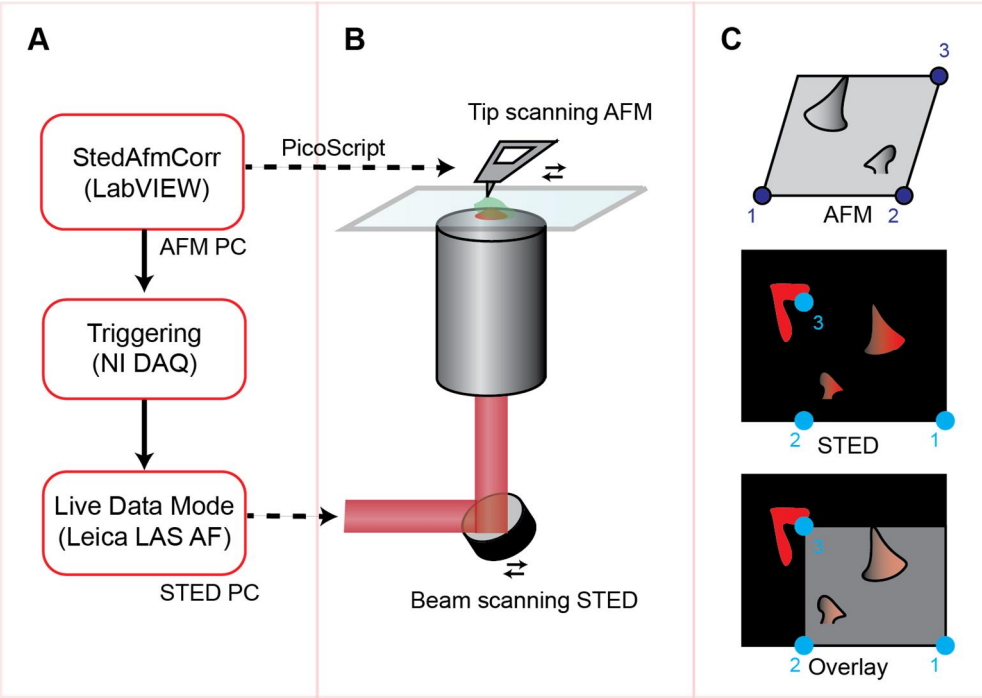

*Figure 3: The Agilent 5500ILM AFM-system was mounted on a Leica TCS STED system with a custom-built stage **B**. StedAfmCorr controls the AFM through the PicoScript API, whereas the STED system is controlled via hardware trigger signals that are generated with a digital I/O card **A**. Landmarks for automatic image alignment in StedAfmCorr were generated by detecting AFM cantilever tip coordinates in confocal reflection images **C** (Chapter 4.2.1). The Figure was reproduced from **III**.*

4.1.3. STED-TEM correlative setup

In (Prabhakar *et al.* Unpublished) a method to correlate STED and transmission electron microscopy (TEM) images was developed. Two separate instruments were used for the imaging: Leica TSC STED (Leica Microsystems, Germany) for STED imaging, with an oil immersion objective lens (Leica STED NA 1.4, 100x), and Jeol JEM-1400 Plus (Jeol Ltd, Japan) for TEM imaging. The samples were first imaged on STED, after which they were prepared for TEM and then re-imaged.

In order to create a reproducible method for finding a common ROI in the two instruments, microscopic identification markings were printed

onto microscope cover glasses, by using dodecanethiol protected gold nanoparticles and inkjet printing with a Dimatrix Materials Printer (DMP-2800, FUJIFILM Dimatrix Inc.). The gold nanoparticles have a good contrast in TEM, and they can be seen in the STED instrument in confocal reflection images or in standard brightfield images.

For image correlation nanodiamonds (NDs) were used as multimodal fiduciary markers. Two registration methods, automatic and semi-automatic were implemented, as discussed in *Chapter 4.2.1*.

4.2. Image reconstruction

4.2.1. Image Registration

The image registration in (**I**) was done semi-manually in ImageJ (version 1.47) 3D Viewer plugin (Schmid *et al.* 2010) by selecting corresponding landmark pairs in the moving and the fixed images to produce a rigid body spatial transform that was then used to resample the moving image. TransformJ plugin (Meijering, Niessen & Viergever 2001) was used prior to registration to resample both of the images to isotropic pixel size, in order to prevent loss of detail during registration. In (**II**) the image registration was done automatically, in our own *SuperTomo* software that was developed as a part of this thesis. The automatic image registration in *SuperTomo* was based on the Mattes mutual information (MMI) similarity metric (Mattes *et al.* 2001, 2003):

$$I(\mu) = -\sum_{\kappa}\sum_{\iota} p(\iota,\kappa \mid \mu)\log\frac{p(\iota,\kappa \mid \mu)}{p_M(\iota \mid \mu)p_F(\kappa)} \qquad \text{(Eq. 4.1.)}$$

, where $I(\mu)$ denotes the Mattes mutual information similarity metric, p_M and p_F are the normalized histograms of moving and fixed images respectively, $p(\iota, \kappa \mid \mu)$ is their joint histogram, μ denotes the transform parameters to be optimized and ι and κ denote the histogram bin indexes for the moving and the fixed image. The joint histogram is maximized during registration. Mutual information based metrics thus, measure the similarity of the histograms

of two images, rather than comparing individual pixel pairs. Such an approach has two benefits: 1° It makes the metric very tolerant to pixel-to-pixel variations, which makes it ideal for the 3D registration of images with anisotropic resolution. 2° Only a small subset of the image pixels are required to calculate the metric, which makes it suitable for use with large images. The MMI based registration method was compared against two previously published methods, based on Normalized Cross Correlation (NCC) and Mean Squared Difference (MS) (Heintzmann & Cremer 2002; Remmele *et al.* 2011). Also the beads based registration methods, which were discussed in *Chapter 2.3.2* were considered, but our STED< data acquisition method does not allow the use of solid-mounted samples. Rigid body spatial transformations were used, because the same geometry was expected in both of the projections. In order to prevent loss of detail, before registration the images were scaled to isotropic pixel size with quintic β-spline interpolation; during registration linear interpolator was used.

In (Prabhakar *et al.* Unpublished) automatic correlative image registration methods were implemented, by expanding *SuperTomo* registration methods to work with 2D images as well. A possibility to use a similarity spatial transform, in addition to a rigid body transform was added, as often TEM sample preparation causes shrinkage of the sample object. In addition, a second, semi-automatic registration method using manually selected landmark pairs and similarity transform was implemented in Matlab (R2011a, Mathworks, USA). The Matlab image registration script is shown in *Chapter 4.5*.

In (**III**) two correlative image registration methods were implemented, both relying on the detection of AFM cantilever tip coordinates in optical reflection images as registration landmarks (*Chapter 4.1.2*). In our *StedAfmCorr* software the landmark detection is semi-automatic: the user is requested to draw a ROI over the region of the cantilever tip location, after which the software calculates the exact coordinates of the tip. Then a perspective spatial transform is calculated to map the AFM image onto the

STED image. The second registration method, which was implemented as a separate ImageJ script, locates the cantilever tip coordinates automatically, after which either an affine or a bilinear spatial transformation is used to map the AFM image onto the STED image. The automatic landmark detection assumes that the tip reflection is the brightest point-source-type detail in the image.

4.2.2. Image Fusion

The image fusion in (**I**) was calculated as follows:

$$o = i_f - (i_f - i_m) \qquad \text{(Eq. 4.2.)}$$

, where i_f and i_m denote the fixed image and the registered moving image respectively, and o is the reconstructed sample object. In essence, co-localizing pixels are kept, whereas non-colocalized pixels reduce to zero. The equation assumes that negative pixel values are not allowed.

In (**II**) a new iterative reconstruction algorithm was introduced:

$$o_{k+1} = \frac{o_k}{N} \sum_{v \in V} \frac{i_v}{o_k \otimes h_v} \otimes h_v^* \prod_{\substack{w \in V \\ w \neq v}} h_v^* \otimes h_w \otimes h_w^* \qquad \text{(Eq. 4.3.)}$$

, where Π denotes multiplication, o_k and o_{k+1} denote the current and the next estimate, N is the number of projections, i_v is an image in the set of projections V, h_v is the PSF corresponding to the i_v, h_v^* its mirrored version and h_w and h_w^* are the regular and mirrored PSFs of all the other views. As shown on the right side of *Equation 4.3* the regular Richardson-Lucy (RL) deconvolution based algorithm (*Chapter 2.3.2, Equation 2.8*) was augmented by a compound-PSF term, which was first proposed for a multiplicative axial tomographic reconstruction algorithm in (Preibisch *et al.* 2014):

$$o_{k+1} = o_k \left(\prod_{v \in V} \frac{i_v}{o_k \otimes h_v} \otimes h_v^* \prod_{\substack{w \in V \\ w \neq v}} h_v^* \otimes h_w \otimes h_w^* \right)^{\frac{1}{N}} \qquad \text{(Eq. 4.4.)}$$

, where the combination of different views is done by multiplication and geometric mean, instead of addition and arithmetic mean (*Equation 4.3*). The idea behind the compound-PSF term, as discussed in (Preibisch *et al.* 2014) is that instead of assuming the independence of the projections, the fusion process is harnessed to take advantage of how all the other views are correlated with the current one. Both of the algorithms were implemented in our *SuperTomo* software, with and without the compound-PSF terms, thus providing altogether four different reconstruction methods. The *SuperTomo* fusion implementation was also directly compared against multiplicative fusion algorithms in the Multiview Reconstruction plugin (Preibisch *et al.* 2014) in Fiji (Continuous release version, http://fiji.sc). The algorithms in *Equations 4.3* and *4.4* were called Efficient Additive and Efficient Multiplicative, whereas their versions without the compound-PSF term were called Regular Additive and Regular Multiplicative respectively.

Two methods were implemented for estimating progress of the fusion over iterations. The changes between two consequent estimates were quantified by τ:

$$\tau = \frac{\sum \left| o_k - o_{k-1} \right|}{\sum o_k} \qquad \text{(Eq. 4.5.)}$$

, where o_k and $o_{k\text{-}1}$ are the current and previous estimates; the differences in each pixel pair are summed to form a single numeric value for τ. The convergence of the fusion algorithm was quantified by ε:

$$\lim_{\substack{v \in V \\ \forall i \in M \\ k \to \infty}} S_i = S \;\Big\|\; S_i = \left(\frac{1}{N} \sum\nolimits_v \frac{i_v}{o_k \otimes h_v} \otimes h_v^* \right)_i \qquad \text{(Eq. 4.6.)}$$

$$0 - \varepsilon \le S \le (0 + \varepsilon) \vee (1 - \varepsilon) \le S \le 1 + \varepsilon$$

, where k is the iteration number, S_i is a pixel in the deconvolution update term that has M pixels.

4.3. Quantitative image analysis

4.3.1. Automatic image quality ranking

In (**IV**) an image quality ranking method and software were introduced. The basic idea is to automatically extract quantitative statistical parameters from a set of images, which can subsequently be used to sort the images within the given dataset, according to their relative quality. *PyImageQualityRanking* software was created for this purpose.

Histogram is a powerful measure of image contrast and dynamic range in the spatial domain. In *PyImageQualityRanking* software the quality of the histogram is estimated by the Shannon entropy measure:

$$H = \sum_i p_i \log \frac{1}{p_i} \qquad \text{(Eq. 4.7.)}$$

, where p_i denotes the normalized image histogram and i is the histogram bin index. The histograms were calculated within masked image regions that contain most detail (highest average intensity), which helped to compensate for the large and varying amount of dark background in fluorescence images.

In addition a plethora of spectral domain measures were extracted, in order to gain a better understanding of the image content, as the spatial histogram measures are mostly limited to quantifying grayscale contrast. For this purpose a one-dimensional power spectrum was calculated from the square of the image FFT (power spectrum) by first adding all rows and columns together and then adding the corresponding "negative" frequencies to the "positive" ones. The image quality ranking method is illustrated in *Figure 4.*

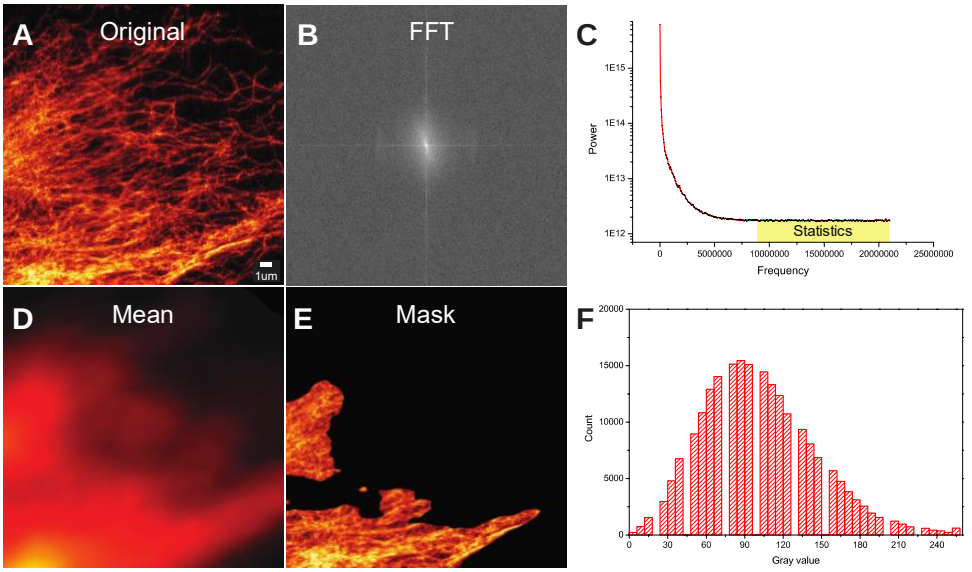

*Figure 4: The working principle of the image-ranking tool is illustrated. In order to extract statistics related to image-structure, noise and blurriness, a frequency domain representation **B** of the original image **A** is computed via Fourier transform, after which it is simplified into a one-dimensional power-spectrum **C**. All the frequency domain statistics are calculated only at the highest frequencies (>40% from maximum). In order to compare the histograms of different images, a spatial mask is first formed by filtering the original image **A** with a large (r=100) uniform mean filter **D**, and then a spatial mask **E** is formed, by selecting the pixel positions in **D**, at which the intensity is higher than 80% of the maximum value. Calculating the histogram **F** from the masked region enables the comparison of images with varying amount of dark background. The illustration was reproduced form **IV**.*

The image quality ranking involves simply taking one or e.g. the average of several of the calculated statistical parameters, and ordering the images based on this parameter value. The parameter values were normalized, by dividing each parameter by its maximum value within the processed dataset. A pseudocode description of the image quality ranking method is given in *Chapter 4.5*.

4.4. Test samples

A fixed cell sample in (**I**) was prepared with HeLa cells, stained with anti-α-tubulin primary mouse antibody (Sigma-Aldrich Clone AA13, lot number 120M4771) and antimouse Atto647N (ATTO-TEC, Germany) secondary

antibody; the same sample was used in (**II**) as well. For (**II**) a second test sample was prepared with MDA-MB-231 cells, stained with anti-α-tubulin primary mouse antibody (Sigma-Aldrich Clone AA13, lot number 120M4771) and antimouse Star635P (Abberior, Germany) secondary antibody. In addition in (**I**) a simple point source sample was prepared with 20nm crimson fluorescent microspheres (Life Technologies Fluoresphere, ThermoFisher Scientific, USA). All the samples were mounted in TDE to allow the placement of the STED< mirror, and the exact tuning of the refractive index.

In (**III**) a point source sample was prepared with 20nm crimson fluorescent microspheres (Life Technologies Fluoresphere, ThermoFisher Scientific, USA) adhered on a poly-l-lysine coated microscope glass coverslip. In addition butterfly cells were used to make a biological test sample by labeling F-actin with phalloidin conjugated ATTO647N (ATTO-TEC, Germany). The samples were mounted in PBS to allow imaging with both STED and AFM.

In (Prabhakar *et al.* Unpublished) nanodiamond particles 10µg/ml were added to HT1080 eGFP cells grown on the coverslips with gold writing (*Chapter 4.1.3*). After live cell STED imaging the cells were fixed, dehydrated, embedded in epoxy (45359 Fluka Epoxy Embedding Medium kit) and cut to 70nm sections for TEM imaging. A simple test sample for estimating the performance of the new image correlation methods was created by adding ND-SiO2 silica coated nanodiamonds on a TEM grid, after which the sample was left to dry.

In (**IV**) vimentin intermediate filaments were labeled in BHK21 cells with a combination of different fixation, permeabilization and blocking methods. Two different primary antibodies, V9 (Sigma) and D21H3 (Cell Signaling Technologies) were applied to each sample preparation method. Two different secondary antibodies, Atto647N (Invitrogen) and Abberior Star635P (Abberior) were used as well. For out-of-focus image detection two

datasets from a high-content-screening time-course experiment of a 3D co-culture of LNCaP tumor cells together with PF179T stromal cells were obtained (Åkerfelt *et al.* 2015). In addition a simulation dataset was generated from regular grayscale photographs.

4.5. Software development

The *SuperTomo* (**II**) software was written in Python (version 2.7). Its image registration features are based on functions in the Insight Toolkit open-source image processing library (Yoo *et al.* 2002), whereas the image fusion part was based on the open-source microscope image deconvolution library IOCBIO-Microscope (Laasmaa *et al.* 2011). The implemented registration and fusion algorithms are discussed in *Chapter 4.2.2* and in (**II**). The basic functionality of the *SuperTomo* as used in (**II**) is described in pseudocode below; in the correlative microscopy application (Prabhakar *et al.* Unpublished) different image registration functions are used (2D images) and the image fusion features are not used, but otherwise the principle is the same.

```
"""
A simplified pseudocode representation of the SuperTomo functionali-
ty.
"""
# Command line options are used extensively in SuperTomo in order to
# give the user a comprehensive way to adjust the behavior of the
# software. The most important options are outlined in the relevant
# sections below
options = GetCommandLineOptions(arguments)

# ITK image I/O functionality is used here.
fixedImage = LoadImage(options.fixedImagePath)
movingImage = LoadImage(options.movingImagePath)

# Image registration
# The behavior of the registration method is mainly defined with the
# following options.
# Registration metric    May be chosen between Mattes mutual infor-
                         mation, Mean Squared Difference and Normal-
                         ized Cross-Correlation.
# Mattes bins/samples    Defines the amount of samples and the num-
                         ber of histogram bins that are used to cre-
                         ate the histograms for Mattes mutual infor-
                         mation metric. The other metrics don't take
                         any parameters.
```

```
# Initial rotation       Defines the initial rotation for the moving
                         image. The program calculates the initial
                         transform from the image moments, but here
                         at least the correct direction of rotation
                         must be defined in order for the initializ-
                         er to work correctly
# Number of Iterations   In case the registration does not converge
                         in reasonable time, the iteration is
                         stopped after a defined number of itera-
                         tions
# Max/min step size      Defines how large or small steps the opti-
                         mizer will take during registration.
# Reg. relax factor      Defines how quickly the optimizer moves
                         into a smaller step size.
# The spatial transformation is always rigid body and a linear
# interpolator is used during registration. The registration
# algorithm is described in detail in Chapter 4.2.1 and in (II).
# A complete list of the command line options is given in the
# software user guide.


if options.register == True:
      spatialTransform = RegisterImages(fixedImage, movingImage,
                                        options)
      SaveTransform(spatialTransform)

# Image Resampling
# The image registration only produces a spatial transformation,
# which is used here to resample the moving image. This way
# the original images are always resampled, whereas before image
# registration various kinds of pre-processing can be applied,
# if necessary. For resampling, a B-spline interpolator can be
# selected with a command line option - by default linear
# interpolator is used here as well.
if options.transform == True or options.register == True:
      if spatialTransform is None:
            spatialTransform = LoadSpatialTranform(
                                        options.transform_path)
      transformedImage = ResampleImage(fixedImage, movingImage,
                                       spatialTransform)
      SaveImage(transformedImage, options.path)

# Image Fusion
# The behavior of the fusion method is mainly defined with the
# following command line options.
# Fusion algorithm       Efficient Additive, Efficient Multiplica-
                         tive, Regular Additive & Regular Multipli-
                         cative. Please see Chapter 4.2.2 or (II)
                         for explanations.
# Max nr. of iterations  The maximum number of deconvolution itera-
                         tions
# Stop tau               The difference between consequent esti-
                         mates at which the fusion iteration stops.
                         By default this is 0.002. (Chapter 4.2.2,
```

```
                              Equation 4.5)
# Convergence epsilon         The degree of convergence at which the it-
                              erations stops (Chapter 4.2.2, Equation
                              4.5)
# rltv lambda                 Total variation regularization (II) can be
                              enabled by defining a non-zero parameter
                              value.
# The fusion algorithm is described in detail in Chapter 4.2.1 and
# in (II). A complete list of the command line options is given in
# the software user guide.

if options.fuse == True:
       # By default a single PSF is used, which means that it also
       # needs to be resampled (rotated) for each view.
       psf1 = LoadImage(options.psfPath)
       if spatialTransform is None:
              spatialTransform = LoadSpatialTransform(
                                          options.transform_path)
       psf2 = RotatePsf(psf1, spatialTransform)

       resultImage = FuseImages([fixedImage, movingImage],
                                [psf1, psf2], options)

       SaveImage(resultImage)
```

The explanation above is limited to a single moving and fixed image pair, which is how *SuperTomo* was implemented, because the STED< data acquisition method only creates two views. Extension to a larger number of views would require repeating the image registration for every projection (loop) and then all the registered views would need to be passed on to the image fusion. The *SuperTomo* software can be downloaded from https://bitbucket.org/sakoho81/supertomo and it has been released under a BSD open-source license.

For (Prabhakar *et al.* Unpublished) a semi-automatic registration method was implemented in Matlab (R2011a, Mathworks, USA), by taking advantage of the Matlab Control Point Selection tool. The image registration script is shown below:

```
% A script for semi-automatic image registration in Matlab

% Open images
fixed_filename = uigetfile('*.tif', 'Specify fixed image');
moving_filename = uigetfile('*.tif', 'Specify moving image');
fixed = imread(fixed_filename);
moving = imread(moving_filename);
```

```
% Register images using control points. First corresponding landmark
% pairs are selected in the Matlab Control Point Selection graphical
% utility (cpselect), after which the moving image is resampled with
% a non-reflective similarity transform.
[moving_points, fixed_points] = cpselect(moving, fixed,'Wait', true);
tform = cp2tform(   moving_points, fixed_points,
                    'nonreflective similarity' );
fixed_info = imfinfo(fixed_filename);
registered = imtransform(  moving, tform,'XData',
                           [1 fixed_info.Width],...
                           'YData',[1 fixed_info.Height]);

% Create and show result image as an RGB overlay
blue = zeros(size(fixed));
result = cat(3, fixed, registered, blue);
imshow(result)

% Save result
output_filename = uiputfile('*.tif', 'Save registration result');
imwrite(result, output_filename);
```

The script can be found in the *SuperTomo* utilities folder, together with several ImageJ utility scripts, implemented in Fiji (Continuous release version, http://fiji.sc).

The *StedAfmCorr* **(III)** software was developed in LabView (2012 Academic Site License version, National Instruments, USA). The Agilent 5500ilm (Keysight Technologies, USA) AFM instrument is controlled via the PicoScript LabView API provided by the microscope manufacturer. In order to allow relatively simple adaptation of the *StedAfmCorr* software to new instruments, the STED and AFM instruments were implemented as polymorphic objects – adding a new instrument only involves implementing the necessary methods in the instrument's class template, after which the main program can select between all available instruments at runtime by dynamic dispatch. The instrument control functionality of the *StedAfmCorr* is described in pseudocode below:

```
"""
A simplified pseudocode representation of the StedAfmCorr instrument
control functionality.
"""
# Initialize the instruments. Here the selected type of
# instrument objects will define how the program
```

```
# in practice works at runtime.
afmInstrument = AgilentAFM(afmParameters)
stedInstrument = LeicaSTED(stedParameters)

# AFM Imaging
# The AFM is controlled via PicoScript API in LabVIEW
# The AFM scan starts by approaching the sample surface
afmInstrument.Approach()
while afmInstrument.InContact() == False:
       waitS(5)

# After the surface has been reached, the AFM image
# can be acquired
afmInstrument.ScanFrame()
while afmInstrument.Complete() == False:
       waitS(5)

# After completing the AFM scan, it may be necessary to
# retract the cantilever in order to prevent it from breaking
# during the STED imaging.
afmInstrument.Retract(distance)

# STED imaging
# STED image sequence proceeds as follows:
# 1. Regular STED image is acquired
# 2. AFM cantilever tip is moved to the first corner
# 3. Landmark image is acquired
# 4. Steps 2. and 3. are repeated for all four corners
# Every time the AFM cantilever is moved to a new position a
# hardware trigger pulse is sent to the STED instrument to initiate
# image acquisition. After the acquisition completes, STEDs sends
# back another trigger pulse. At the end of the sequence the STED
# image must be saved manually, to make the image correlation possi-
ble.
stedInstrument.RunSequence()
while stedInstrument.Complete() == False:
       waitS(5)
```

The STED-AFM correlative image registration functionality was implemented in the main *StedAfmCorr* software in LabVIEW, and as a separate ImageJ script in Fiji (Continuous release version, http://fiji.sc). The landmark based image registration in the Fiji script was implemented with the TurboReg (Thevenaz, Ruttimann & Unser 1998) plugin. The image registration algorithm in both of the implementations is similar, and it is explained in pseudocode below:

```
"""
A simplified pseudocode representation of the StedAfmCorr
Image registration functionality.
"""
```

```
# The AFM image can be fetched directly from the instrument
# or alternatively it can be loaded from a file. STED images
# are always loaded from a file, because there is no way to
# access the Leica LAS AF software.
afmImagePath = GetPath("Select AFM image file")
stedImagePath = GetPath("Select STED image file")
landmarkPath = GetPath("Select landmark image file")

afmImage = LoadAfmImage(afmImagePath)
stedImage = LoadStedImage(stedImagePath)
landmarkImages = LoadImageSeries(landmarkPath)

# Finding landmarks
# Here the software searches for the landmark features in the
# selected landmark images. In the ImageJ script this is done
# automatically, whereas in the LabVIEW implementation of
# StedAfmCorr the user is prompted to draw a rectangular ROI over
# a landmark position, after which the software finds the exact
# position within the ROI.
landmarkCoordinates = FindLandmarks(landmarkImages, options)

# In order to match the landmark coordinates with the image corners,
# the detected coordinates must be sorted. The sorting assumes that
# the corners are in the same order than in the reference image, i.e.
# the AFM image should not be flipped or rotated more than 90°.
landmarkCoordinates = SortCoordinates(landmarkCoordinates)

# The reference positions can be calculated from the AFM image.
imageCornerCoordinates =   [[0,0],
                            [0, afmImage.Height()],
                            [afmImage.Width(), 0],
                            [afmImage.Width(), afmImage.Height()]
                           ]
# Image registration
# Resample the AFM image. At the output the AFM image is the same
# size as the STED image, although the original AFM image only
# covers a small part of the STED FOV. This is done in order to make
# it possible to overlay the multimodal images. Perspective spatial
# transform is used in StedAfmCorr, whereas Affine transform is used
# in the ImageJ script.
resultImage = Register(stedImage, afmImage, landmarkCoordinates,
imageCornerCoordinates)

# Show and save results. The results are shown as a RGB overlay im-
age.
ShowResults(stedImage, afmImage, resultImage)
SaveImage(resultImage, filename)
```

The *StedAfmCorr* software and the ImageJ image registration script can be downloaded from https://bitbucket.org/sakoho81/stedafmcorr, and it has been released under a BSD open-source license.

The *PyImageQualityRanking* (**IV**) software was written in Python (version 2.7), by taking advantage of standard Scientific Python open-source software libraries. Numpy and SciPy were used to implement all the image processing and analysis features, whereas Pandas was used to implement methods to process the results (data sorting by parameter value, parameter calculations, parameter normalization etc.). Matplotlib was used for image visualization, as well as to produce mathematical plots. In many quantitative microscopy applications time lapse recordings are made, which means that the order of the images should not be changed – therefore the data sorting features in *PyImageQualityRanking* software do not actually change the order of the images, but instead the software creates a separate data file with the image names and parameter values, which can be safely modified, without risk of compromising the original image data. The basic functionality of the *PyImageQualitRanking* software is described in pseudocode below; the image analysis method is explained in detail in *Chapter 4.3.1* and in (**IV**).

```
"""
A simplified pseudocode representation of the PyImageQualityRanking
functionality.
"""
options = GetCommandLineOptions(arguments)

# Parameter extraction
# In the default directory mode all the files within a given input
# directory are analyzed. The directory is given as a command line
# parameter.
if options.directory == True:
       # The results are saved into a CSV data file. The data
       # contains the image filenames as well as all the parameter
       # values.
       dataFile = NewCsvFile(options.outputPath)
       dataFile.WriteHeader("Filename", "Entropy", "SpectralSTD" ...)

       for image in fileList(options.path):
              # Only images are considered
              if not IsImageFile(image):
                     continue
              imageFile = OpenImage(image)

              # The program extracts a number of parameters in
              # spatial and spectral domains, as discussed in Chapter
              # 4.3.1. All the parameters are calculated
              # here and then they are saved as a new row to the
              # data file.
```

```
                spatialParams = GetSpatialParameters(imageFile)
                spectralParams = GetSpectralParameters(imageFile)
                dataFile.writeRow([spatialParams, spectralParams])

        dataFile.Save()

# Parameter calculations
# Here the above produced data file is processed using functions in
# the Pandas library. All the parameter values are normalized to the
# highest parameter value within the dataset. In addition certain
# new parameter values, for example CV or invSTD (1 - spectral
# domain STD) are calculated here.
if options.analyze == True:
        dataFile = ReadCsv(options.outputPath)

        newValues = analyzeData(dataFile)
        dataFile.Append(newValues)
        dataFile.Save()

# Parameter ranking
# The sorting option enables the image ranking. The sorting is
# separate from the analysis functionality, because often times one
# would like to sort the data several times by a different parameter
# type. Once the data file has been created the sorting can be run
# as many times as one desires.
if options.sort == True:
        if dataFile is None:
                dataFile = ReadCsv(options.outputPath)

        # Sort by parameter value
        dataFile = SortData(dataFile, options.sortingParameter)
        # The changes are always saved to enable direct observation of
        # the results in the CSV file, as well as to make it possible
        # to use the ranking results for selecting or discarding
        # certain images
        dataFile.Save()

        # Show a chosen number of images from the top and the bottom
        # of the new ranking.
        bestImages = dataFile.GetBest(options.numberToPlot)
        worstImages = dataFile.GetWorst(options.numberToPlot)
        plot(bestImages)
        plot(worstImages)
```

The *PyImageQualityRanking* software can be downloaded from https://bitbucket.org/sakoho81/pyimagequalityranking and it has been released under a BSD open-source license.

5. RESULTS & DISCUSSION

In this chapter the results in the original publications (**I-IV**) are summarized and discussed. Also some unpublished results are shown (Prabhakar *et al.* Unpublished). The original publications discuss the results in detail.

5.1. Axial tomographic super-resolution

A new data acquisition method STED< for axial tomographic super-resolution microscopy was developed in (**I**). *SuperTomo* software for reconstructing STED< datasets was introduced in (**II**).

5.1.1. Data acquisition

The STED< data acquisition, as discussed in *Chapter 4.1.1* involves the placement of a small mirror on top of the sample in order to gain access to an oblique view to it; the precise tilt angle of the mirror does not have to be known exactly, as the image reconstruction algorithm in *SuperTomo* automatically estimates it from the data. This makes acquiring axial projections with STED< possible even with quite rudimentary instrumentation: a standard commercial STED microscope was used in our work, without any modifications to the microscope optics on the optical path.

In (**I**) a sample of 20nm nanoparticles, as well as an entire fixed HeLa cell was imaged. Our measurements showed that only minimal deterioration of the SNR and resolution could be observed in the mirror-reflected projection, when compared to the regular STED image. Moreover, we did not experience any problem in acquiring axial projections from a MDB-MB-231 cell sample (**II**) with a very limited SNR. In (Deguchi *et al.* 2015) we even successfully acquired the STED< projection through a thin, highly scattering layer of bone in a osteoclast cell sample, which underlines the robustness of the simple data acquisition method – this is thanks to the 2D depletion donut that is used in our microscope, which is much less sensitive to aberrations than the 3D depletion donut (Deng *et al.* 2009). No geometrical

distortions of image detail were observed in any of our images.

However, while STED< allows the simple acquisition of axial tomographic projections, its applicability is limited to relatively thin and transparent samples that in addition must be mounted in a liquid mounting medium, with a nearly uniform refractive index that matches that of the immersion oil. This is due to the need to refocus to the sample, by first going through the sample itself, when acquiring the oblique projection through the mirror. Moreover the working distance in the STED oil immersion objective is limited to 90µm, which in addition to the sample thickness, also sets limitations to the lateral size of the sample, as in the oblique STED< view, axial movement is translated into lateral. Developing a sample rotation based data acquisition method would solve these problems – such a method would potentially enable 3D super-resolution STED imaging in thick specimen, up to twice the working distance of the objective, as discussed in *Chapter 2.3.1*. This is particularly interesting, as the applications of the current 3D STED techniques are largely limited to thin samples, or sample surfaces, due to the fast deterioration of the 3D donut in depth.

Axial tomographic imaging is limited mostly to fixed samples, because several views of the sample must be generated in a sequential manner, which takes time, and therefore movements in a live-cell sample easily distort the image geometry. As discussed in (Krzic *et al.* 2012), simultaneous acquisition from both sides of the sample can help, when working with large specimen. Such an optical arrangement, combined with recently proposed ultra-fast raster scan methods (Duocastella, Vicidomini & Diaspro 2015; Schneider *et al.* 2015; Kong *et al.* 2015) and a real-time image reconstruction (Schmid & Huisken 2015), could open up the possibility to image relatively large dynamic (live) biological samples in STED.

5.1.2. Image reconstruction

The manual image registration in (**I**) only allowed us to demonstrate the axial tomographic STED< reconstruction on the 20nm Crimson fluorescent

nanoparticle images. As shown in *Figure 5* the reconstructed image has significantly improved axial detail. HeLa cell images were registered as well, but manual alignment of image details was not sufficiently precise to allow image fusion; therefore in (**I**) the axial projections are shown side by side. *SuperTomo* software (**II**) solved this issue by implementing methods for automatic 3D image registration and fusion.

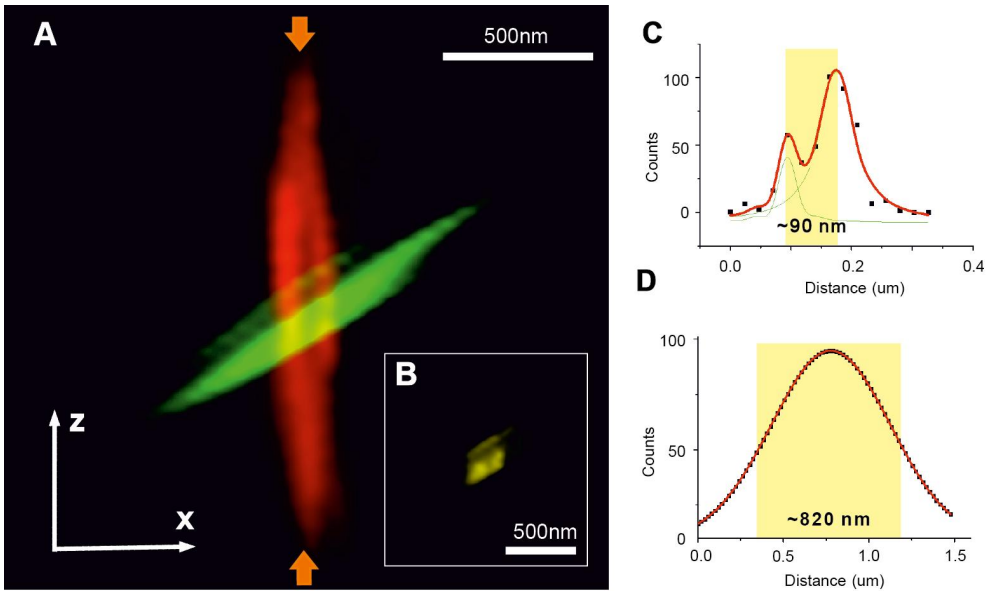

Figure 5: A single point source was extracted from the 20nm Crimson fluorescent nanoparticle images. In **A** *an image of apparently a single nanoparticle is shown in the manually registered STED and STED< views, and in* **B** *the fusion result is shown. Line profile plots in the axial direction, as indicated by arrows in* **A**, *reveal significantly increased axial detail in the fused image* **C**, *when compared with the regular STED image* **D**. *The Figure was modified from* **I**.

Out of the three image registration methods implemented in *SuperTomo* only the one based on MMI worked with all of our test images. NCC and MS based registration methods both suffered from excessive memory requirements, when working with large images. In addition, MS based registration did not behave well with the low-SNR MDB-MB-231 cell sample. MMI based registration was consistently the fastest of the three methods, and required the least amount of memory. Only 500,000 spatial samples were required to register HeLa cell images with ~700,000,000 pixels (STED< projection: 1024x1024x648 pixels), which is less than one per mille of the data! The automatic image registration was able to correct ~50° rotational and ~4µm translational offset between the projections, simultaneously. Three dimensional renderings of the STED and STED< projections before and after registration are shown in *Figure 6A-B*, and the registration is shown to align the two projections to visual limits in *Figure 6C*.

Due to the explained limitations of manual image registration, image fusion in (**I**) was only shown with the nanoparticle sample. The simple image reconstruction in any case, allowed us to produce tomograms, with apparent axial resolution in <100nm range, as shown in *Figure 5C*, an approximately six-fold improvement over the regular STED image.

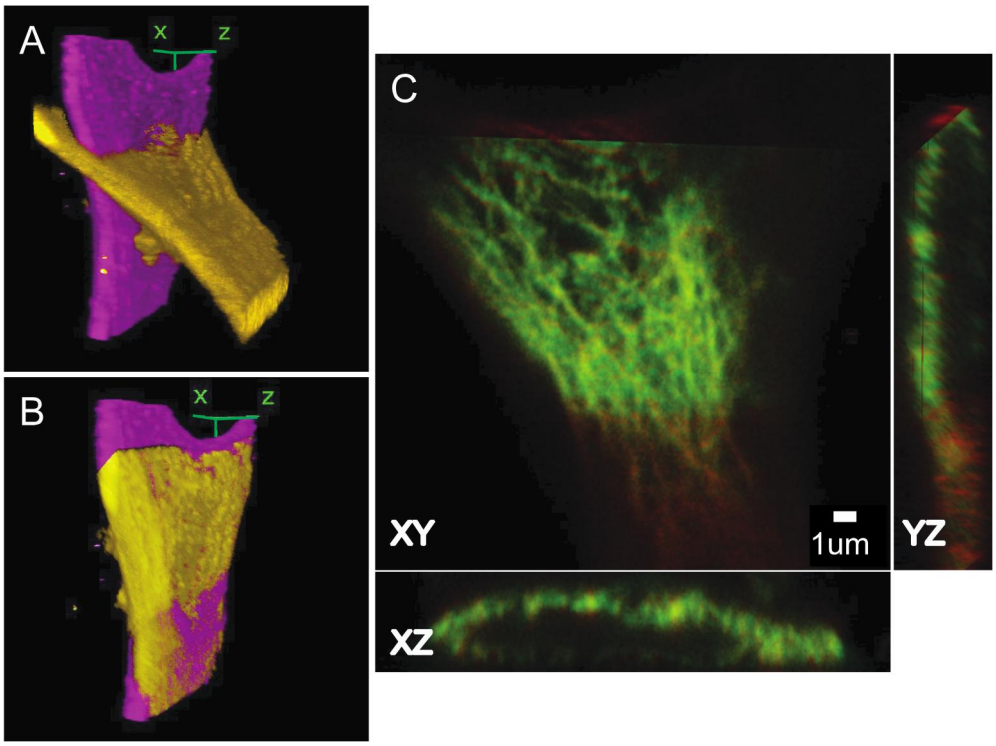

*Figure 6: The two STED< projections before **A** and after B the automatic image registration are shown. In **C** axial views of the registration results show that the two views (STED red, STED< green) are aligned to visual limits. It is also evident from **C** that the STED< projection only contains a part of the cell – this did not prevent succesfull image registration. The Figure was modified from **II**.*

In (**II**) our Efficient Additive reconstruction algorithm was consistently shown to produce the sharpest results, whereas the Regular Additive algorithm maintained a slightly higher SNR. The fusion results with the Efficient Additive and the Regular Additive algorithms are shown in *Figure 7B,E* for the HeLa cell images, and in *Figure 8B,C* for the MDB-MB-231 cell images. The results show clearly improved apparent axial detail when compared to the regular STED images (*Figure 7A* and *Figure 8A)*, as illustrated by line-profile plots in *Figure 7C-D*. The *SuperTomo* software consistently produced results with richer axial detail and was four-to-five times faster than the previously published Multiview Reconstruction plugin in Fiji (Preibisch *et al.* 2014). The results of image fusion with the Efficient Multi-

plicative algorithm in the Multiview Reconstruction plugin are shown in *Figure 7F* for the HeLa cell images and in *Figure 8D* for the MDB-MB-231 cell images. The *SuperTomo* image fusion worked fine even with the limited SNR MDB-MB-231 cell images, whereas the Multiview Reconstruction plugin lost a lot of detail with the HeLa cell images and did not work at all with MDB-MB-231 cell images. Additive algorithms were preferred throughout, as they were significantly faster than the multiplicative ones, whereas the results were practically identical. No difference in convergence time was observed either. Regularization was not used, because enabling it only blurred finer detail in the fusion results.

The MMI based registration was shown to produce good results with very limited amount of samples, even with very noisy images. This makes the registration implementation in *SuperTomo* very attractive for use with large 3D images. The beads based registration algorithms that were discussed in *Chapter 2.3.2* are a good alternative, whenever adding and immobilizing nanoparticles to be used as registration landmarks is reasonable, or even possible. Using such methods with STED, would require the implementation of a data acquisition method that works with solid mounted samples, based on sample rotation for example, as discussed in *Chapter 5.1.1*. *SuperTomo* enables similar fast, memory-efficient image registration, based on the image details, without posing limitations to the instrumentation or need for additional sample preparation and data segmentation/cleaning steps.

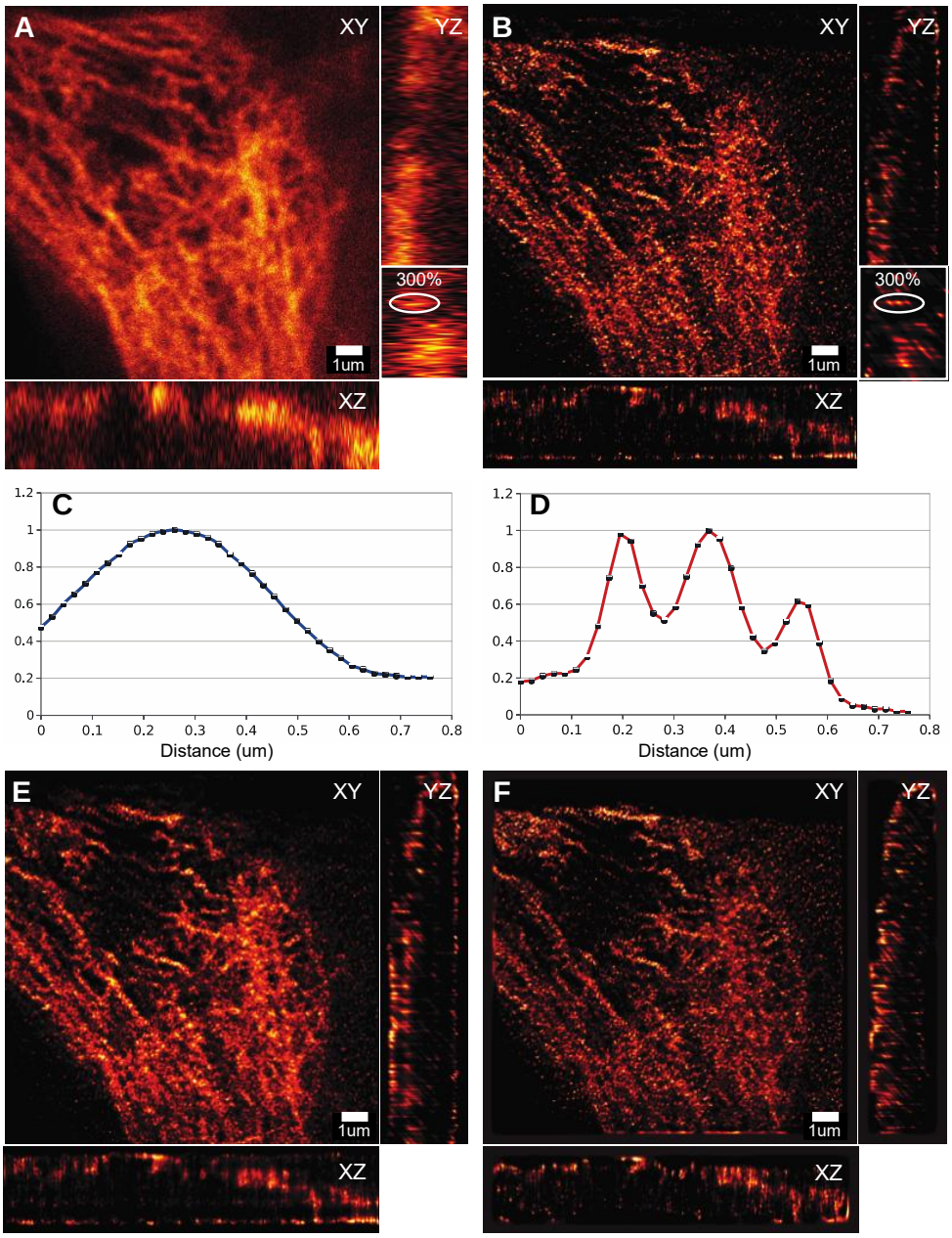

*Figure 7: The regular STED image of the HeLa cell is shown in **A**, and the fusion results with the Efficient Additive and the Regular Additive algorithms, as well as with the Efficient Multiplicative algorithm in the Multiview Reconstruction Fiji plugin are shown in **B**, **E** and **F** respectively. The fusion results show clearly improved apparent axial detail, as shown in line profile plots **C** and **D** that were calculated from corresponding positions in **A** and **B** as illustrated in the 300% zoomed image sections. The Figure was reproduced from **II**.*

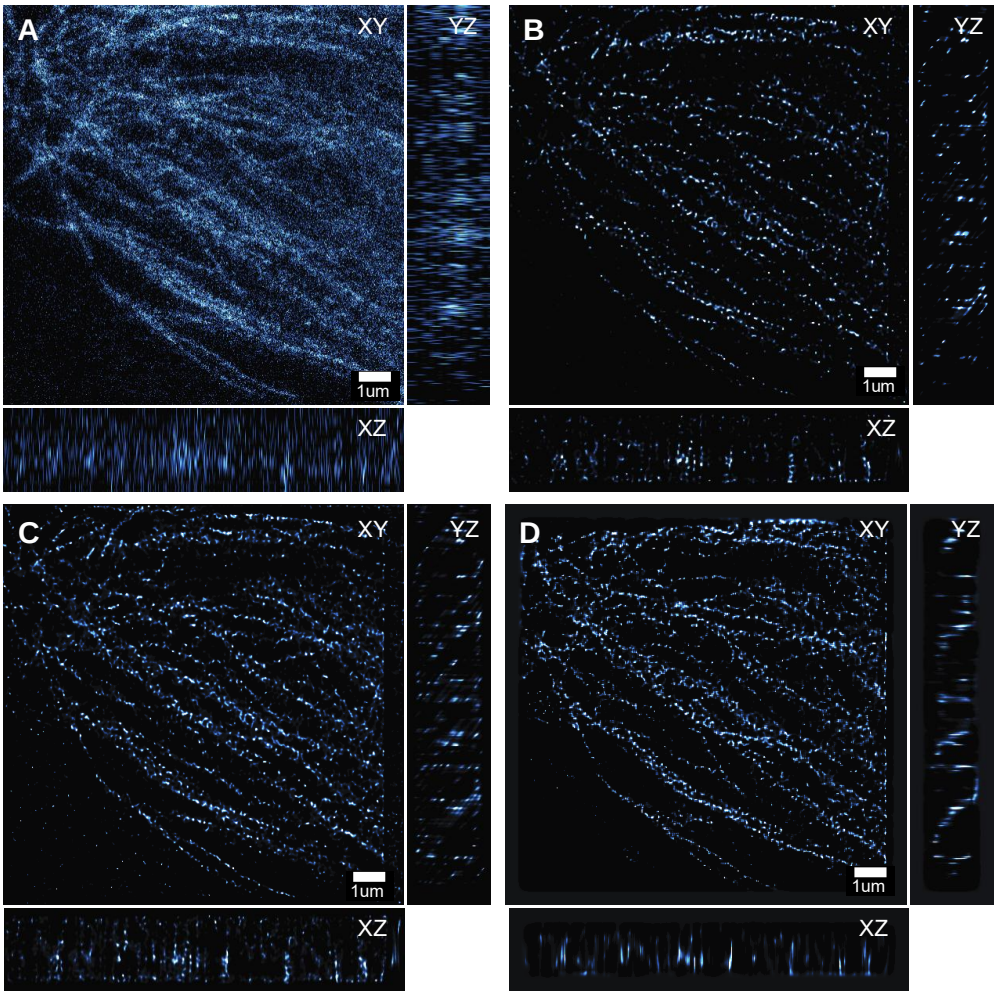

*Figure 8: The regular STED image of the MDB-MB-231 cell is shown in **A**, and the fusion results with the Efficient Additive and the Regular Additive algorithms, as well as with the Efficient Multiplicative algorithm in the Multiview Reconstruction Fiji plugin are shown in **B**, **C** and **D** respectively. The axial detail can be seen to almost match the lateral in **B** and **C**, whereas in **D** there seems to be no major improvement over **A**. The Figure was reproduced from **II**.*

It is also important to note that the *SuperTomo* image registration works with physical distances, which means that if needed, it is possible to downscale (shrink) the images before registration and then use produced spatial transform to resample the full size images at the end. In (**II**) it was shown that identical registration results could be obtained with 60%

downscaled HeLa cell images with those obtained with the full size images. Such an approach gives additional options for optimizing the memory requirements and time consumption of image registration tasks, when working with very large images.

Currently the STED< method only employs two projections, and therefore the *SuperTomo* image fusion has been particularly implemented for such task. With two projections, calculating the image fusion for the entire image at once is a reasonable approach, as the memory requirements are still moderate. However, in case very large images were to be used, or if a data acquisition method able to produce a larger amount of projections was implemented, the fusion algorithm would need to be run on image subsets (blocks). Such an approach has been outlined, for example in (Nagy & O'Leary 1997). Dividing the reconstruction problem into blocks would also have another benefit: it would allow parallelizing the fusion calculation, for example on a GPU. Recently such algorithms were proposed for fusing multi-view lightsheet images (Preibisch *et al.* 2014; Schmid & Huisken 2015).

5.2. Correlative super-resolution microscopy

StedAfmCorr software for correlative STED-AFM microscopy was introduced in (**III**), and a method for correlating STED-TEM images was presented in (Prabhakar *et al.* Unpublished). In (**III**) subjects related to instrument control and image correlation are covered, whereas in (Prabhakar *et al.* Unpublished), from the software point-of-view, the focus is exclusively on the image correlation problem.

5.2.1. Instrument control

StedAfmCorr enabled the synchronization of data acquisition between two commercial, previously completely incompatible STED and AFM instruments. In (**III**) it was shown how the *StedAfmCorr* instrument control features could be used to automatically acquire an image sequence, containing STED and AFM frames, as well as the necessary landmark images for image

registration. The simple hardware-trigger-based integration to the Leica LAS AF Live Data Mode application was observed to work well, although a dedicated API would certainly allow for a more robust control of the STED instrument, and it would also remove the need to manually save the STED images, in order to make them available for *StedAfmCorr*. In addition in (**III**) we discussed that *StedAfmCorr* software would be extended beyond imaging applications as well: for example in force spectroscopy or live-cell stimulation experiments one could guide the AFM data acquisition/stimulation, by first marking structures of interest in the STED image and then using the *StedAfmCorr* to drive the AFM to those positions and to synchronize the data acquisition with STED. At the time of the writing of this thesis, the software development to enable these advanced features is still a work in progress.

5.2.2. Image correlation

The landmark based STED-AFM image registration in (**III**) was demonstrated to work with a nanoparticle sample and a fixed butterfly cell sample, as shown in *Figure 9A*. The semi-automatic landmark detection in LabVIEW requires a small amount of manual work for image correlation, but on the other hand an additional measure of robustness is added for situations in which there are several point-like objects in the landmark images, and thus automatic landmark detection could not be used. As shown in *Figure 9C* also the fully automatic image registration, implemented in ImageJ can cope with a considerable amount of noise in the landmark images, and thus should work in most practical cases. In the nanoparticle overlay in *Figure 9B* it can be seen that there is some tens of nanometers offset in the registered images, which can be attributed to a variety of factors: e.g. non-linearity in the AFM instrument, possible optical aberrations in STED or inaccuracies in determining the precise position of the AFM cantilever tip. A more precise correlation could be achieved by acquiring landmarks inside the AFM frame as well, which would allow for compensation of image deformations. Alternatively fiduciary markers, i.e. nanoparticles could be added to the sample, but it

would contaminate the AFM data, and the AFM tip might also move the nanoparticles during imaging. For most practical purposes, the accuracy of the current results is completely sufficient, and its simplicity helps to keep the focus on the actual imaging, rather than the image correlation task.

The automatic correlative STED-TEM registration implementation in *SuperTomo* (Prabhakar *et al.* Unpublished) was demonstrated to work well with simple nanodiamond particle images (*Figure 10A*), as well as with HT1080 eGFP cell images (*Figure 10B*). With the semi-automatic Matlab registration script nearly identical results were obtained. The *SuperTomo* registration with the rigid body spatial transform appears to produce more reasonable results than the scalable similarity transform enabled image registration – for a better evaluation, images with more common landmarks should be obtained; the Matlab registration results are very reasonable, but of course only depend on the subjective point-pair selections, which may vary from one registration attempt to the next. Automatic registration tools are more robust in this respect, but they of course require at least some extent of similarity in the two images, in order to work properly. It is quite surprising, how well the *SuperTomo* registration methods work with the HT1080 eGFP images, considering that the images appear quite different to the eye. The cell images demonstrate some practical difficulties in STED-TEM correlative imaging. TEM images show much lower number of nanodiamonds, which partially is due to a considerably smaller slice thickness – 70nm in TEM as opposed to ~600nm in STED, and the TEM sample preparation also seems to harm the nanodiamonds – this is a practical sample preparation issue that we are currently dealing with. It is also quite difficult to determine the exact same axial slice for correlation, because the contrast in the STED and the TEM images is quite different. These kinds of issues could be addressed by working with complete 3D volumes instead of single 2D images. Algorithmically this would involve first registering the individual EM sections to form a 3D volume, after which it could be registered with a STED

stack. Such an algorithm would be rather straightforward to implement in *SuperTomo*, as the 2D and 3D registration methods already exist – adding such a feature may well be the next step in the correlative STED-TEM image registration development in *SuperTomo*. Alternatively a beads based registration algorithm, such as (Preibisch *et al.* 2010) could be used, because fiducicary markers are nearly always used in LM-EM correlative imaging.

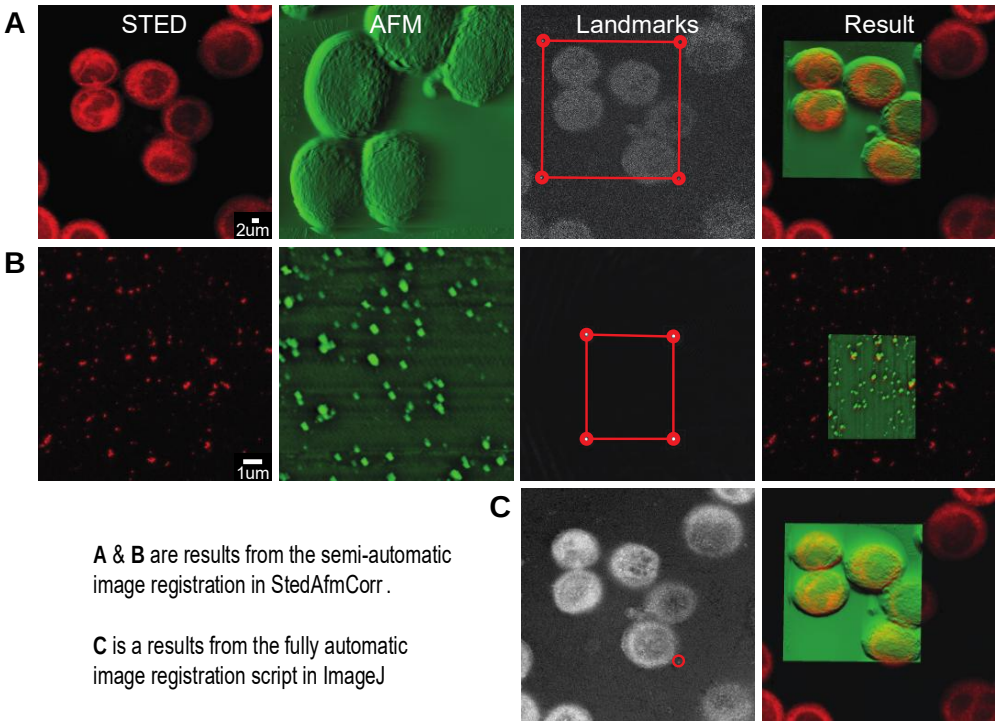

Figure 9: The STED-AFM image correlation results are shown with the Butterfly cell images in **A** *nd* **C**. *The semi-automatic image registration in StedAfmCorr* **A** *and the automatic image registration with the ImageJ script* **C** *produce nearly identical results. As shown in* **C** *the automatic landmark detection can tolerate a considerable amount of noise. The nanoparticle overlay in* **B** *shows a small offset between the STED and AFM images, which could be caused by a variety of factors – the accuracy should me more than sufficient for visualization purposes. The Figure was modified from* ***III***.

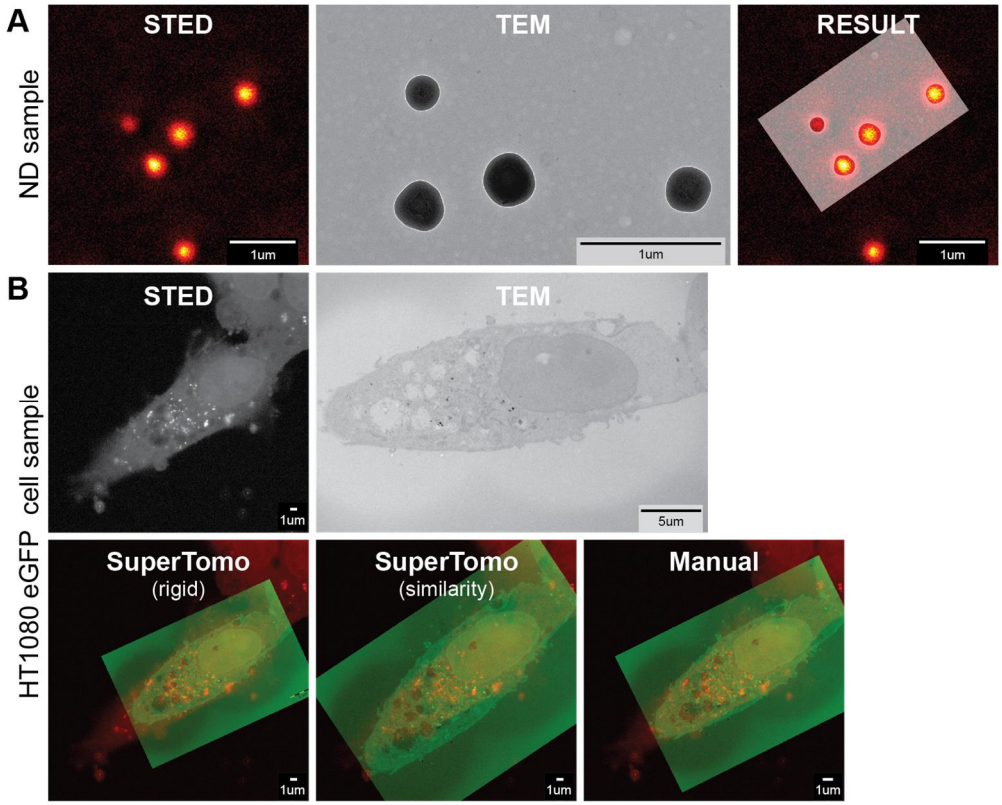

Figure 10: The STED-TEM image correlation results are shown with the simple nanodiamond test sample **A** *and the HT1080 eGFP live cell sample, with added nanodiamond particles* **B**. *With the test sample the SuperTomo automatic image registration exactly matches the STED and TEM images. With the live cell sample SuperTomo automatic registration with rigid body non-deformable spatial transformation appears to produce the most reasonable results, whereas the scalable transform enabled registration appears to exaggerate the scaling slightly – the manual (semi-automatic) registration in Matlab works well as well, but it requires the manual selection of corresponding landmark pairs, which may produce a slightly different result at every registration attempt. (Prabhakar* et al. *Unpublished).*

5.3. Microscope image quality ranking

PyImageQualityRanking software (**IV**) can be used to rank images within image datasets according to their relative quality. In (**IV**) we demonstrated how our method can be used to find out-of-focus images in automatic quantitative HCS experiment, as well as to find the highest quality images in a regular STED microscopy dataset.

5.3.1. Can computer see a good image?

Averaging of two statistical parameters: inverse of the power spectrum standard deviation (invSTD) and spatial entropy was shown to be a suitable multi-parametric measure for image goodness in a STED microscopy dataset. The image quality ranking results by *PyImageQualityRanking* software exactly matched the subjective selections. Examples of the ranking results can be seen in *Figure 11B*. The entropy is a good measure of image contrast, but it was not able to find the best images alone – the invSTD measure was required in order to take the image detail into account as well. As to why the invSTD correlates so well with good images is a bit unclear; it appears that good images have a more continuous power spectrum, whereas noisy/dotty images put a greater emphasis on high frequencies, and low frequencies are attenuated. The invSTD measure favors images with least amount of noise, which could be a problem if there are blurry images in the dataset as well – in such case the good images may end up between the noisy and the blurred images in the ranking.

Combining the simple quality ranking method in *PyImageQualityRanking* software with an automatic pattern recognition method (Shamir *et al.* 2010) would make it possible to find good images, with the desired content. This might enable a form of automatic image understanding (Huang & Murphy 2004) – or at least a lot of computational effort would be saved in large-scale experiments, as the segmentation could be focused on the good quality images. Aside from the large-scale quantitative experiments, being

able to quickly find suitable images for analysis is a great comfort in any day-to-day microscopy image analysis task, because the time can be spent on analyzing the data, rather than on finding a needle in a haystack. Applications could also be found in other fields of science, such as medical imaging, automated inspection or aerial and satellite imagery.

5.3.2. Finding outliers

The simulation photography dataset (*Figure 12*) revealed that the power-spectrum standard deviation (STD) measure in *PyImageQualityRanking* software is a great metric of image blurriness. Therefore it was used alone to detect out-of-focus images in the HCS datasets – a few examples of the results are shown in *Figure 11B*. It was shown in (**IV**) that out-of-focus images could be found with both fluorescence and phase contrast. The STD measure was also able to separate perfectly focused images from those with only slightest amount of blur – although in some cases in which the datasets contained images with very different amount of content however, the nearly empty perfectly focused images were sometimes mixed with these slightly blurry images. This could be taken into account in the ranking calculations, for example by using the number of pixels above a certain threshold value as a normalization parameter. Also without such measure all clearly out-of-focus images were found in all our test datasets. Although our image quality ranking method does not require a reference image, manually selecting a good in-focus image to be used as a reference, would enable the use of the method as an autofocus metric, for example. The power spectrum STD is relatively simple to calculate, which means that the measurement could be done in real time, even on embedded instrument control hardware. Our simple image quality ranking method could also easily be added to high-content microscopy data analysis workflows, to enable automatic detection of out-of-focus images that should be left out from the quantitative calculations.

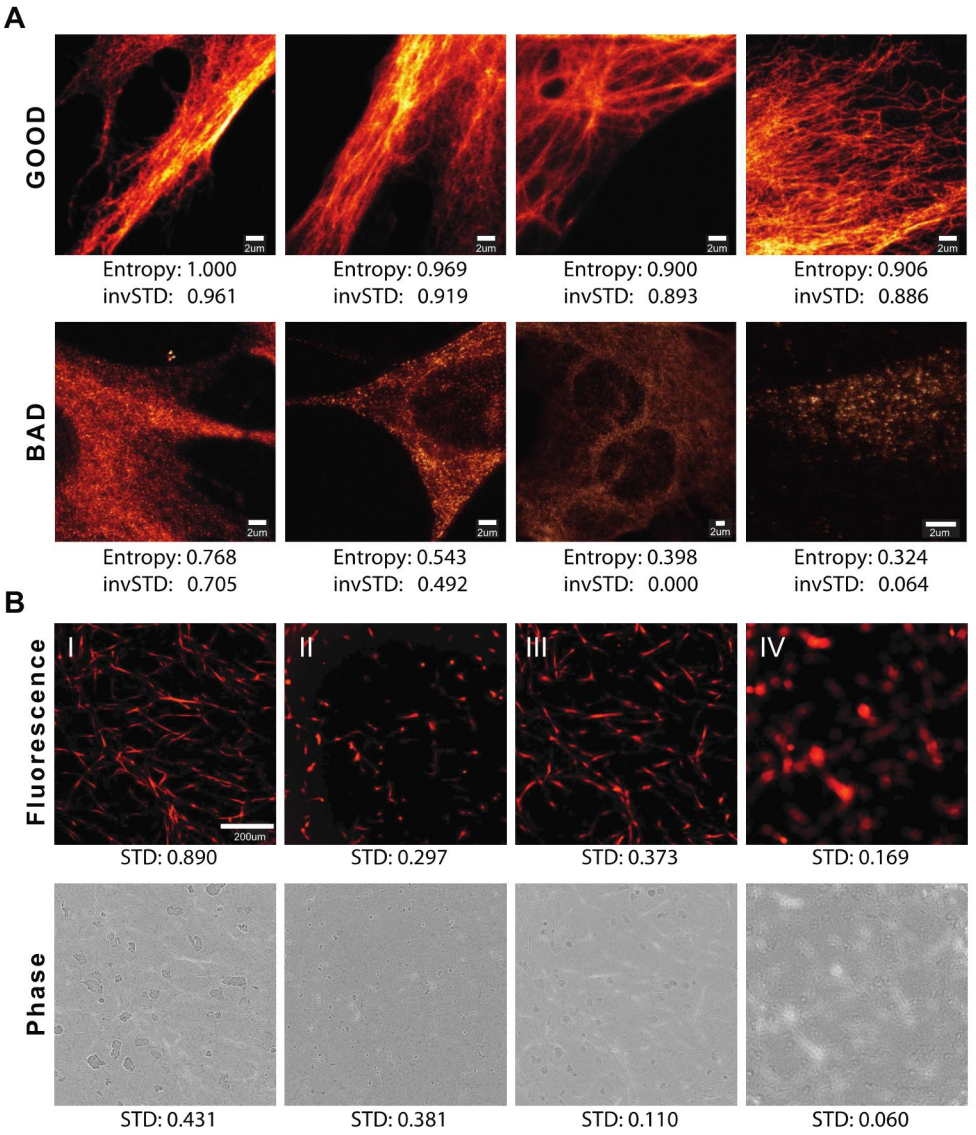

*Figure 11: The four best and the four worst images from the STED image dataset are shown in A. Both the spatial entropy and the inverse of the spectral domain STD (invSTD) measures correlate well with the image quality. Four example images with both fluorescence and phase contrast from the HCS dataset are shown in **B**. The spectral domain STD measure correlates well with the quality of focus – however, as can be seen in the fluorescence images, sometimes images with very little content II may get mixed with slightly blurry images III; the same problem is not seen with phase-contrast images, because the image content does not change as drastically. Thus, the out-of-focus image ranking mehtod works best with images with similar amount of content. The Figure was reproduced from **IV**.*

Figure 12: The simulation photograph dataset together with image quality ranking parameter values for each image are shown. The spectral domain STD measure can be seen to correlate quite linearly with the amount of blur and noise, whereas the spectral domain Mean responds more aggressively to both blur and noise. The STD measure is thus better suited for use as a metric. The Figure was reproduced from **IV**.

6. CONCLUSIONS

In this thesis a glimpse was given into the increasingly complex world of (super-resolution) microscopy, with particular focus on software tools. These tools play a key role in all aspects of microscopy today – and their importance in the coming years is certainly going to increase. Software enables the construction of high-resolution, high-speed and high-content instruments: all these features are required when microscopy little-by-little transitions from single cells into more complex and even living model systems.

In (**I** and **II**) a tomographic STED super-resolution microscopy technique was introduced. Nearly isotropic apparent 3D super-resolution was achieved in a standard 2D STED system. The *SuperTomo* tomographic reconstruction software compared favorably with a current state-of-the-art method (Preibisch *et al.* 2014). Our axial tomographic method should enable 3D super-resolution STED imaging in relatively thick biological specimen, which is out-of-reach of the current STED techniques, due to the fast deterioration of the axial depletion shape in depth. In addition, our initial results indicate that the *SuperTomo* image registration functionality could prove useful in correlative microscopy applications (Prabhakar *et al.* Unpublished).

In (**III**) a software tool for STED-AFM correlative imaging was introduced. Our software tool enables integrated control of the two instruments and also provides methods to correlate the imaging results. No similar tools, to our knowledge, have been introduced before in literature. Our software should enable new kinds of STED-AFM correlative microscopy applications: one could for instance use the AFM to stimulate receptors on living cells, while simultaneously following the signaling events on the STED in real-time.

In (**IV**) an image quality ranking method was introduced for microscopy. No similar method, to our knowledge, exist in the literature. Image

quality assessment in microscopy, is currently largely limited to the detection of out-of-focus images in automated quantitative imaging experiments. Our simple method was shown to work well in detecting out-of-focus images, and it worked equally well in detecting images with good detail and contrast (good images). Currently our method does not integrate any pattern recognition functionality – combining our image quality ranking method with such a tool should enable the detection of good images with structures of interest, a form of automated image understanding. Due to the increasing complexity of microscopy experiments and image datasets, such automated tools will be essential in the near future.

Three new open-source bioimage informatics software tools were introduced. While each of the tools were initially designed for a very specific purpose, for example *SuperTomo* software shows how one software can be found useful in two very different applications (**II** and (Prabhakar *et al.* Unpublished)). All the introduced software tools have been released under open-source licenses, and they are conveniently distributed through online code repositories, from which anyone can download and use them, and maybe in the ideal case, even add new features. This is the fundamental idea behind open-source software, and also behind good scientific practices, which emphasize the reproducibility of scientific results. Taking the thought a little further, recent attempts like the Arduino project (https://www.arduino.cc/), will hopefully one day make it possible to open-source scientific hardware designs as well – most of the times the embedded instrument control software is inseparable from the hardware, and open-sourcing the software alone thus makes little sense. This would certainly be a great resource for setting up new imaging systems or laboratories.

In an attempt to improve the usability of the introduced software tools (Carpenter, Kamentsky & Eliceiri 2012), we intend to integrate at least some of the features of *SuperTomo* and *PyImageQualityRanking* in Bi-

oimageXD (Kankaanpää *et al.* 2012), which will make the developed tools available also to scientists with limited computer science knowledge, in a convenient GUI application – and it will hopefully also prevent our efforts from being lost in the sea of nifty little software tools that no one ends up using.

The development of the *SuperTomo* software is currently continuing, very much along the lines of the discussion in *Chapters 5.1.2* and *5.2.2*: tomographic reconstruction features are to be expanded to work with a larger number of projections and with extremely large image datasets, and STED-TEM automatic image correlation is to be expanded in a way to accommodate ambitious multi-modal biological experiments. *PyImageQualityRanking* software has many possible application areas, but it remains to be seen, which kind of applications benefit from it the most. *StedAfmCorr* STED-AFM instrument control software will hopefully soon be expanded to allow interesting live cell applications; it would be interesting to see as well, how well the software integrates with other types of instruments than those available to us – maybe the open-source science community will give us a hand in that.

.

ACKNOWLEDGEMENTS

The thesis work was carried out at the Laboratory of Biophysics, Department of Cell Biology and Anatomy, University of Turku.

I would like to thank the Turku Doctoral Programme of Molecular Medicine (TuDMM) for providing me with ample travel grants that allowed me to attend conferences and to make interesting scientific visits.

I would like to thank Professor Pekka Hänninen for giving me the time and freedom to grow as a scientist. Your support was always there, when it was needed, but most of the time you just trusted me to make my own choices, which I highly appreciate. In addition, the opportunity to work as a teacher ever since the beginning of my career at the university, has been a pleasure, and it has also helped me significantly to develop professionally.

I would like to thank my thesis reviewers Professor Ulla Ruotsalainen and Associate Professor Juha Toivonen. Your comments helped me to significantly improve the text.

I would like to thank my thesis advisory board members Associate Professor Juha Toivonen and Dr. Daniel Abankwa. Thank you for your support and comments.

I would like to thank Professor John Eriksson, who has played a key role on my scientific career. Thank you for all the trust, the endless ideas and the always positive spirit – and for using your international contacts to create opportunities that could not have been realized otherwise. Photoacoustic microscopy technique, which thanks to you I had the opportunity to learn at the Northwestern University, although not shown on the pages of this book, will certainly have an important part in my future scientific career.

I would like to thank my colleagues Dr. Takahiro Deguchi and Dr. Tuomas Näreoja (currently with Karolinska Institutet): without you two I would have probably never finished my thesis, maybe I would not have even

started. It has been a true pleasure working with you throughout the years, and growing up together, as colleagues and friends. We made a good team, and I am looking forward to our future collaborations.

I would also like to thank all my other colleagues at the Laboratory of Biophysics. Elena Tcarenkova, thank you for your efforts with the Photoacoustic microscopy development, and also for reviewing my thesis. It has been a true pleasure working with you, and I am looking forward to realizing all our microscopy development ideas. Elnaz Fazeli, thank you for your work with the STED sample preparation optimization. Without your work, I would have probably never come up with the idea for image quality ranking. Janne Kulpakko and Neeraj Prabhakar, thank you for your friendship and all the great ideas. Eija Martikkala, a special thank you for your all around positive attitude and happiness – you are a true help on the dark autumn mornings. Anita Rozwandowicz-Jansen, we have really never worked together, but it has been nice knowing you ever since my first day at the Laboratory of Biophysics. Thank you also to all my former colleagues.

I would like to thank my current and former Master's students, Divyendu Gould, Kari Vienola & Madis Löhmus, who also play(ed) an important role in the microscopy development group. Divyendu, thank you for taking up the challenge of continuing the tomographic STED development; I am sure we will achieve great results. Kari and Madis, thank you for the work with the STED-AFM correlative microscopy development.

I would like to thank the Imaging Boyz: Pasi Kankaanpää, Jouko Sandholm, Markku Saari, Tibor Veres and Jari Korhonen. It has been a pleasure working with you in various kinds of scientific and Turku Bioimaging related projects. Thank you also to the current and former Turku Bioimaging coordinators: Inga, Petra, Joanna, Maritta and Eeva – you have made my life much easier, especially on teaching-related matters, on several occasions.

I would like to thank my parents Jouni and Eija, as well as my brother Joonas and my sister Hanna. I also want to thank my parents in law Riccardo and Giovanna, as well as my sister in law Lara. You are all so very important to me. Thank you for your years of support and encouragement.

I would like to thank my wife Elisa Bertieri. I don't know how I would survive through a day without your support, let alone finishing a PhD. Thank you for all the years of support, for tolerating the long working hours and for believing in me.

Turku, February 2016

Sami Koho

REFERENCES

Abrahamsson, S., Chen, J., Hajj, B., Stallinga, S., Katsov, A.Y., Wisniewski, J., Mizuguchi, G., Soule, P., Mueller, F., Darzacq, C.D., Darzacq, X., Wu, C., Bargmann, C.I., Agard, D.A., Dahan, M. & Gustafsson, M.G.L. (2013) Fast multicolor 3D imaging using aberration-corrected multifocus microscopy. *Nature Methods*, **10**, 60–63.

Agard, D.A., Hiraoka, Y., Shaw, P. & Sedat, J.W. (1989) Fluorescence microscopy in three dimensions. *Methods in Cell Biology*, **30**, 353–377.

Åkerfelt, M., Bayramoglu, N., Robinson, S., Toriseva, M., Schukov, H.-P., Härmä, V., Virtanen, J., Sormunen, R., Kaakinen, M., Kannala, J., Eklund, L., Heikkilä, J. & Nees, M. (2015) Automated tracking of tumor-stroma morphology in microtissues identifies functional targets within the tumor microenvironment for therapeutic intervention. *Oncotarget*, **in press**.

Ambrose, E.J. (1956) A Surface Contact Microscope for the study of Cell Movements. *Nature*, **178**, 1194–1194.

Aslund, N., Carlsson, K., Liljeborg, A. & Majlof, L. (1983) PHOIBOS, a microscope scanner designed for micro-fluorometric applications, using laser induced fluorescence. *Proceedings of the Third Scandinavian Conference on Image Analysis, Studentliteratur*, p. 338.

Axelrod, D. (1981) Cell-substrate contacts illuminated by total internal reflection fluorescence. *The Journal of Cell Biology*, **89**, 141–145.

Baddeley, D., Jayasinghe, I.D., Cremer, C., Cannell, M.B. & Soeller, C. (2009) Light-Induced Dark States of Organic Fluochromes Enable 30 nm Resolution Imaging in Standard Media. *Biophysical Journal*, **96**, L22–L24.

Benninger, R.K.P. & Piston, D.W. (2013) Two-Photon Excitation Microscopy for the Study of Living Cells and Tissues. *Current protocols in cell biology / editorial board, Juan S. Bonifacino ... [et al.]*, **0 4**, Unit–4.1124.

Betzig, E. (1995) Proposed method for molecular optical imaging. *Optics Letters*, **20**, 237.

Betzig, E., Patterson, G.H., Sougrat, R., Lindwasser, O.W., Olenych, S., Bonifacino, J.S., Davidson, M.W., Lippincott-Schwartz, J. & Hess, H.F. (2006) Imaging Intracellular Fluorescent Proteins at Nanometer Resolution. *Science*, **313**, 1642–1645.

Bewersdorf, J., Schmidt, R. & Hell, S.W. (2006) Comparison of I5M and 4Pi-microscopy. *Journal of Microscopy*, **222**, 105–117.

de Boer, P., Hoogenboom, J.P. & Giepmans, B.N.G. (2015) Correlated light and electron microscopy: ultrastructure lights up! *Nature Methods*, **12**, 503–513.

Bradl, J., Hausmann, M., Ehemann, V., Komitowski, D. & Cremer, C. (1992) A tilting device for three-dimensional microscopy: application to in situ imaging of interphase cell nuclei. *Journal of Microscopy*, **168**, 47–57.

Bray, M.-A., Fraser, A.N., Hasaka, T.P. & Carpenter, A.E. (2012) Workflow and Metrics for

Image Quality Control in Large-Scale High-Content Screens. *Journal of Biomolecular Screening*, **17**, 266–274.

Brázdilová, S. l. & Kozubek, M. (2009) Information content analysis in automated microscopy imaging using an adaptive autofocus algorithm for multimodal functions. *Journal of Microscopy*, **236**, 194–202.

Bretschneider, S., Eggeling, C. & Hell, S.W. (2007) Breaking the Diffraction Barrier in Fluorescence Microscopy by Optical Shelving. *Physical Review Letters*, **98**, 218103.

Cannell, M.B., McMorland, A. & Soeller, C. (2006) Image Enhancement by Deconvolution. *Handbook Of Biological Confocal Microscopy* (ed J.B. Pawley), pp. 488–500. Springer US.

Caplan, J., Niethammer, M., Taylor II, R.M. & Czymmek, K.J. (2011) The power of correlative microscopy: multi-modal, multi-scale, multi-dimensional. *Current Opinion in Structural Biology*, **21**, 686–693.

Carlsson, K. & Åslund, N. (1987) Confocal imaging for 3-D digital microscopy. *Applied Optics*, **26**, 3232.

Carpenter, A.E., Kamentsky, L. & Eliceiri, K.W. (2012) A call for bioimaging software usability. *Nature Methods*, **9**, 666–670.

Carrington, W.A. (1990) Image restoration in 3-D microscopy with limited data., pp. 72–83.

Castello, M., Diaspro, A. & Vicidomini, G. (2014) Multi-images deconvolution improves signal-to-noise ratio on gated stimulated emission depletion microscopy. *Applied Physics Letters*, **105**, 234106.

Chacko, J.V., Canale, C., Harke, B. & Diaspro, A. (2013a) Sub-Diffraction Nano Manipulation Using STED AFM. *PLoS ONE*, **8**, e66608.

Chacko, J.V., Harke, B., Canale, C. & Diaspro, A. (2014) Cellular level nanomanipulation using atomic force microscope aided with superresolution imaging. *Journal of Biomedical Optics*, **19**, 105003–105003.

Chacko, J.V., Zanacchi, F.C. & Diaspro, A. (2013b) Probing cytoskeletal structures by coupling optical superresolution and AFM techniques for a correlative approach. *Cytoskeleton*, **70**, 729–740.

Chang, Y.-W., Chen, S., Tocheva, E.I., Treuner-Lange, A., Löbach, S., Søgaard-Andersen, L. & Jensen, G.J. (2014) Correlated cryogenic photoactivated localization microscopy and cryo-electron tomography. *Nature Methods*, **11**, 737–739.

Chen, B.-C., Legant, W.R., Wang, K., Shao, L., Milkie, D.E., Davidson, M.W., Janetopoulos, C., Wu, X.S., Hammer, J.A., Liu, Z., English, B.P., Mimori-Kiyosue, Y., Romero, D.P., Ritter, A.T., Lippincott-Schwartz, J., Fritz-Laylin, L., Mullins, R.D., Mitchell, D.M., Bembenek, J.N., Reymann, A.-C., Böhme, R., Grill, S.W., Wang, J.T., Seydoux, G., Tulu, U.S., Kiehart, D.P. & Betzig, E. (2014) Lattice light-sheet microscopy: Imaging molecules to embryos at high spatiotemporal resolution. *Science*, **346**, 1257998.

Churchman, L.S., Ökten, Z., Rock, R.S., Dawson, J.F. & Spudich, J.A. (2005) Single molecule high-resolution colocalization of Cy3 and Cy5 attached to macromolecules

measures intramolecular distances through time. *Proceedings of the National Academy of Sciences of the United States of America*, **102**, 1419–1423.

Cogswell, C.J., Larkin, K.G. & Klemm, H.U. (1996) Fluorescence microtomography: multiangle image acquisition and 3D digital reconstruction., pp. 109–115.

Conchello, J.-A., Kim, J.J. & Hansen, E.W. (1994) Enhanced three-dimensional reconstruction from confocal scanning microscope images II Depth discrimination versus signal-to-noise ratio in partially confocal images. *Applied Optics*, **33**, 3740.

Conrad, C., Wünsche, A., Tan, T.H., Bulkescher, J., Sieckmann, F., Verissimo, F., Edelstein, A., Walter, T., Liebel, U., Pepperkok, R. & Ellenberg, J. (2011) Micropilot: automation of fluorescence microscopy-based imaging for systems biology. *Nature Methods*, **8**, 246–249.

Deguchi, T., Koho, S.V., Näreoja, T., Peltonen, J. & Hänninen, P. (2015) Tomographic STED microscopy to study bone resorption. *Proceedings of SPIE*, p. 93301M–93301M–6.

Deng, S., Liu, L., Cheng, Y., Li, R. & Xu, Z. (2009) Investigation of the influence of the aberration induced by a plane interface on STED microscopy. *Optics Express*, **17**, 1714–1725.

Denk, W., Strickler, J. & Webb, W. (1990) Two-photon laser scanning fluorescence microscopy. *Science*, **248**, 73–76.

Dey, N., Blanc-Feraud, L., Zimmer, C., Roux, P., Kam, Z., Olivo-Marin, J.-C. & Zerubia, J. (2006) Richardson–Lucy algorithm with total variation regularization for 3D confocal microscope deconvolution. *Microscopy Research and Technique*, **69**, 260–266.

Duocastella, M., Vicidomini, G. & Diaspro, A. (2015) Simultaneous multiplane imaging for 3D confocal microscopy using high-speed z-scanning multiplexing., p. 93300Q–93300Q–5.

Eliceiri, K.W., Berthold, M.R., Goldberg, I.G., Ibáñez, L., Manjunath, B.S., Martone, M.E., Murphy, R.F., Peng, H., Plant, A.L., Roysam, B., Stuurman, N., Swedlow, J.R., Tomancak, P. & Carpenter, A.E. (2012) Biological imaging software tools. *Nature Methods*, **9**, 697–710.

Fernandez, R., Das, P., Mirabet, V., Moscardi, E., Traas, J., Verdeil, J.-L., Malandain, G. & Godin, C. (2010) Imaging plant growth in 4D: robust tissue reconstruction and lineaging at cell resolution. *Nature Methods*, **7**, 547–553.

Firestone, L., Cook, K., Culp, K., Talsania, N. & Preston, K. (1991) Comparison of autofocus methods for automated microscopy. *Cytometry*, **12**, 195–206.

Fish, D.A., Brinicombe, A.M., Pike, E.R. & Walker, J.G. (1995) Blind deconvolution by means of the Richardson–Lucy algorithm. *Journal of the Optical Society of America A*, **12**, 58.

Folling, J., Bossi, M., Bock, H., Medda, R., Wurm, C.A., Hein, B., Jakobs, S., Eggeling, C. & Hell, S.W. (2008) Fluorescence nanoscopy by ground-state depletion and single-molecule return. *Nat Meth*, **5**, 943–945.

Gelles, J., Schnapp, B.J. & Sheetz, M.P. (1988) Tracking kinesin-driven movements with nanometre-scale precision. *Nature*, **331**, 450–453.

Girish, C.M., Binulal, N.S., Anitha, V.C., Nair, S., Mony, U. & Prasanth, R. (2009) Atomic force microscopic study of folate receptors in live cells with functionalized tips. *Applied Physics Letters*, **95**, 223703–223703–3.

Gould, T.J., Burke, D., Bewersdorf, J. & Booth, M.J. (2012) Adaptive optics enables 3D STED microscopy in aberrating specimens. *Optics Express*, **20**, 20998–21009.

Grotjohann, T., Testa, I., Leutenegger, M., Bock, H., Urban, N.T., Lavoie-Cardinal, F., Willig, K.I., Eggeling, C., Jakobs, S. & Hell, S.W. (2011) Diffraction-unlimited all-optical imaging and writing with a photochromic GFP. *Nature*, **478**, 204–208.

Gustafsson, M.G. (1999) Extended resolution fluorescence microscopy. *Current Opinion in Structural Biology*, **9**, 627–628.

Gustafsson, M.G.L. (2005) Nonlinear structured-illumination microscopy: Wide-field fluorescence imaging with theoretically unlimited resolution. *Proceedings of the National Academy of Sciences of the United States of America*, **102**, 13081–13086.

Gustafsson, M.G.L., Agard, D.A. & Sedat, J.W. (1995) Sevenfold improvement of axial resolution in 3D wide-field microscopy using two objective lenses., pp. 147–156.

Gustafsson, Agard & Sedat. (1999) I5M: 3D widefield light microscopy with better than 100 nm axial resolution. *Journal of Microscopy*, **195**, 10–16.

Gustafsson, M.G.L., Shao, L., Carlton, P.M., Wang, C.J.R., Golubovskaya, I.N., Cande, W.Z., Agard, D.A. & Sedat, J.W. (2008) Three-Dimensional Resolution Doubling in Wide-Field Fluorescence Microscopy by Structured Illumination. *Biophysical Journal*, **94**, 4957–4970.

Hänninen, P.E., Hell, S.W., Salo, J., Soini, E. & Cremer, C. (1995) Two-photon excitation 4Pi confocal microscope: Enhanced axial resolution microscope for biological research. *Applied Physics Letters*, **66**, 1698–1700.

Hänninen, P.E., Soini, E. & Hell, S.W. (1994) Continuous wave excitation two-photon fluorescence microscopy. *Journal of Microscopy*, **176**, 222–225.

Harke, B., Chacko, J.V., Haschke, H., Canale, C. & Diaspro, A. (2012) A novel nanoscopic tool by combining AFM with STED microscopy. *Optical Nanoscopy*, **1**, 3.

Heilemann, M., van de Linde, S., Schüttpelz, M., Kasper, R., Seefeldt, B., Mukherjee, A., Tinnefeld, P. & Sauer, M. (2008) Subdiffraction-Resolution Fluorescence Imaging with Conventional Fluorescent Probes. *Angewandte Chemie International Edition*, **47**, 6172–6176.

Heintzmann, R. & Cremer, C. (2002) Axial tomographic confocal fluorescence microscopy. *Journal of Microscopy*, **206**, 7–23.

Heintzmann, R., Kreth, G. & Cremer, C. (2000) Reconstruction of Axial Tomographic High Resolution Data from Confocal Fluorescence Microscopy: A Method for Improving 3D FISH Images. *Analytical Cellular Pathology*, **20**, 7–15.

Hell, S.W. (2004) Strategy for far-field optical imaging and writing without diffraction limit. *Physics Letters A*, **326**, 140–145.

Hell, S.W., Jakobs, S. & Kastrup, L. (2003) Imaging and writing at the nanoscale with focused visible light through saturable optical transitions. *Applied Physics A: Materials Science & Processing*, **77**, 859–860.

Hell, S.W. & Kroug, M. (1995) Ground-state-depletion fluorscence microscopy: A concept for breaking the diffraction resolution limit. *Applied Physics B*, **60**, 495–497.

Hell, S.W., Lindek, S., Cremer, C. & Stelzer, E.H.K. (1994) Measurement of the 4Pi-confocal point spread function proves 75 nm axial resolution. *Applied Physics Letters*, **64**, 1335–1337.

Hell, S.W., Schrader, M., Bahlmann, K., Meinecke, F., Lakowicz, J.R. & Gryczynski, I. (1995) Stimulated emission on microscopic scale: Light quenching of Pyridine 2 using a Ti:sapphire laser. *Journal of Microscopy*, **180**, RP1–RP2.

Hell, S. & Stelzer, E.H.K. (1992) Properties of a 4Pi confocal fluorescence microscope. *Journal of the Optical Society of America A*, **9**, 2159.

Hell, S.W. & Wichmann, J. (1994) Breaking the diffraction resolution limit by stimulated emission: stimulated-emission-depletion fluorescence microscopy. *Optics Letters*, **19**, 780–782.

Hess, S., Girirajan, T. & Mason, M. (2006) Ultra-High Resolution Imaging by Fluorescence Photoactivation Localization Microscopy. *Biophysical Journal*, **91**, 4258–4272.

Hofmann, M., Eggeling, C., Jakobs, S. & Hell, S.W. (2005) Breaking the diffraction barrier in fluorescence microscopy at low light intensities by using reversibly photoswitchable proteins. *Proceedings of the National Academy of Sciences of the United States of America*, **102**, 17565–17569.

Holmes, T.J. (1992) Blind deconvolution of quantum-limited incoherent imagery: maximum-likelihood approach. *Journal of the Optical Society of America. A, Optics and Image Science*, **9**, 1052–1061.

Holmes, T.J., Biggs, D. & Abu-Tarif, A. (2006) Blind Deconvolution. *Handbook Of Biological Confocal Microscopy* (ed J.B. Pawley), pp. 468–487. Springer US.

Holmes, T.J. & Liu, Y.-H. (1991) Acceleration of maximum-likelihood image restoration for fluorescence microscopy and other noncoherent imagery. *Journal of the Optical Society of America A*, **8**, 893.

Huang, K. & Murphy, R.F. (2004) From Quantitative Microscopy to Automated Image Understanding. *Journal of biomedical optics*, **9**, 893–912.

Huang, B., Wang, W., Bates, M. & Zhuang, X. (2008) Three-Dimensional Super-Resolution Imaging by Stochastic Optical Reconstruction Microscopy. *Science*, **319**, 810–813.

Huisken, J., Swoger, J., Bene, F.D., Wittbrodt, J. & Stelzer, E.H.K. (2004) Optical Sectioning Deep Inside Live Embryos by Selective Plane Illumination Microscopy. *Science*, **305**, 1007–1009.

Huisken, J., Swoger, J., Lindek, S. & Stelzer, E.H.K. (2006) Selective Plane Illumination Microscopy. *Handbook Of Biological Confocal Microscopy* (ed J.B. Pawley), pp. 672–679.

Springer US.

Inoué, S. (1990) Foundations of Confocal Scanned Imaging in Light Microscopy. *Handbook of Biological Confocal Microscopy* (ed J.B. Pawley), pp. 1–14. Springer US.

Jansson, P.A., Hunt, R.H. & Plyler, E.K. (1970) Resolution Enhancement of Spectra. *Journal of the Optical Society of America*, **60**, 596.

Johnson, E., Seiradake, E., Jones, E.Y., Davis, I., Grünewald, K. & Kaufmann, R. (2015) Correlative in-resin super-resolution and electron microscopy using standard fluorescent proteins. *Scientific Reports*, **5**, 9583.

Juette, M.F., Gould, T.J., Lessard, M.D., Mlodzianoski, M.J., Nagpure, B.S., Bennett, B.T., Hess, S.T. & Bewersdorf, J. (2008) Three-dimensional sub–100 nm resolution fluorescence microscopy of thick samples. *Nature Methods*, **5**, 527–529.

Kankaanpää, P., Paavolainen, L., Tiitta, S., Karjalainen, M., Päivärinne, J., Nieminen, J., Marjomäki, V., Heino, J. & White, D.J. (2012) BioImageXD: an open, general-purpose and high-throughput image-processing platform. *Nature Methods*, **9**, 683–689.

Keller, P.J., Schmidt, A.D., Wittbrodt, J. & Stelzer, E.H.K. (2011) Digital Scanned Laser Light-Sheet Fluorescence Microscopy (DSLM) of Zebrafish and Drosophila Embryonic Development. *Cold Spring Harbor Protocols*, **2011**, pdb.prot065839.

Kim, D., Deerinck, T.J., Sigal, Y.M., Babcock, H.P., Ellisman, M.H. & Zhuang, X. (2015) Correlative Stochastic Optical Reconstruction Microscopy and Electron Microscopy. *PLoS ONE*, **10**, e0124581.

Klar, T.A. & Hell, S.W. (1999) Subdiffraction resolution in far-field fluorescence microscopy. *Optics Letters*, **24**, 954.

Klar, T.A., Jakobs, S., Dyba, M., Egner, A. & Hell, S.W. (2000) Fluorescence microscopy with diffraction resolution barrier broken by stimulated emission. *Proceedings of the National Academy of Sciences*, **97**, 8206–8210.

Kong, L., Tang, J., Little, J.P., Yu, Y., Lämmermann, T., Lin, C.P., Germain, R.N. & Cui, M. (2015) Continuous volumetric imaging via an optical phase-locked ultrasound lens. *Nature Methods*, **12**, 759–762.

Kopek, B.G., Shtengel, G., Xu, C.S., Clayton, D.A. & Hess, H.F. (2012) Correlative 3D superresolution fluorescence and electron microscopy reveal the relationship of mitochondrial nucleoids to membranes. *Proceedings of the National Academy of Sciences*, **109**, 6136–6141.

Krishnamurthi, V., Liu, Y.-H., Bhattacharyya, S., Turner, J.N. & Holmes, T.J. (1995) Blind deconvolution of fluorescence micrographs by maximum-likelihood estimation. *Applied Optics*, **34**, 6633.

Krzic, U. (2009) *Multiple-View Microscopy with Light-Sheet Based Fluorescence Microscope*. Dissertation, Ruperto-Carola University, Heidelberg, Germany.

Krzic, U., Gunther, S., Saunders, T.E., Streichan, S.J. & Hufnagel, L. (2012) Multiview light-sheet microscope for rapid in toto imaging. *Nature Methods*, **9**, 730–733.

Kukulski, W., Schorb, M., Welsch, S., Picco, A., Kaksonen, M. & Briggs, J.A.G. (2012) Chapter 13 - Precise, Correlated Fluorescence Microscopy and Electron Tomography of Lowicryl Sections Using Fluorescent Fiducial Markers. *Methods in Cell Biology*, Correlative Light and Electron MIcroscopy (ed T.M.-R. and P. Verkade), pp. 235–257. Academic Press.

Laasmaa, M., Vendelin, M. & Peterson, P. (2011) Application of regularized Richardson–Lucy algorithm for deconvolution of confocal microscopy images. *Journal of Microscopy*, **243**, 124–140.

Laksameethanasan, D., Brandt, S.S., Engelhardt, P., Renaud, O. & Shorte, S.L. (2008) A Bayesian reconstruction method for micro-rotation imaging in light microscopy. *Microscopy Research and Technique*, **71**, 158–167.

Li, D., Shao, L., Chen, B.-C., Zhang, X., Zhang, M., Moses, B., Milkie, D.E., Beach, J.R., Hammer, J.A., Pasham, M., Kirchhausen, T., Baird, M.A., Davidson, M.W., Xu, P. & Betzig, E. (2015) Extended-resolution structured illumination imaging of endocytic and cytoskeletal dynamics. *Science*, **349**, aab3500.

Ljosa, V. & Carpenter, A.E. (2009) Introduction to the Quantitative Analysis of Two-Dimensional Fluorescence Microscopy Images for Cell-Based Screening. *PLoS Computational Biology*, **5**.

Löschberger, A., Franke, C., Krohne, G., Linde, S. van de & Sauer, M. (2014) Correlative super-resolution fluorescence and electron microscopy of the nuclear pore complex with molecular resolution. *Journal of Cell Science*, **127**, 4351–4355.

Lucy, L.B. (1974) An iterative technique for the rectification of observed distributions. *The Astronomical Journal*, **79**, 745.

Manley, S., Gillette, J.M., Patterson, G.H., Shroff, H., Hess, H.F., Betzig, E. & Lippincott-Schwartz, J. (2008) High-density mapping of single-molecule trajectories with photoactivated localization microscopy. *Nature Methods*, **5**, 155–157.

Markey, M.K., Boland, M.V. & Murphy, R.F. (1999) Toward objective selection of representative microscope images. *Biophysical Journal*, **76**, 2230–2237.

Masich, S., Ostberg, T., Norlén, L., Shupliakov, O. & Daneholt, B. (2006) A procedure to deposit fiducial markers on vitreous cryo-sections for cellular tomography. *Journal of Structural Biology*, **156**, 461–468.

Mattes, D., Haynor, D.R., Vesselle, H., Lewellen, T.K. & Eubank, W. (2003) PET-CT image registration in the chest using free-form deformations. *IEEE Transactions on Medical Imaging*, **22**, 120–128.

Mattes, D., Haynor, D.R., Vesselle, H., Lewellyn, T.K. & Eubank, W. (2001) Nonrigid multimodality image registration. *Proceedings of SPIE 4322*, pp. 1609–1620.

McNally, J.G., Karpova, T., Cooper, J. & Conchello, J.A. (1999) Three-Dimensional Imaging by Deconvolution Microscopy. *Methods*, **19**, 373–385.

Meijering, E.H.W., Niessen, W.J. & Viergever, M.A. (2001) Quantitative evaluation of convolution-based methods for medical image interpolation. *Medical Image Analysis*, **5**,

111–126.

Minsky, M. (1961) Microscopy apparatus.

Minsky, M. (1988) Memoir on inventing the confocal scanning microscope. *Scanning*, **10**, 128–138.

Monserrate, A., Casado, S. & Flors, C. (2014) Correlative Atomic Force Microscopy and Localization-Based Super-Resolution Microscopy: Revealing Labelling and Image Reconstruction Artefacts. *ChemPhysChem*, **15**, 647–650.

Mudry, E., Belkebir, K., Girard, J., Savatier, J., Moal, E.L., Nicoletti, C., Allain, M. & Sentenac, A. (2012) Structured illumination microscopy using unknown speckle patterns. *Nature Photonics*, **6**, 312–315.

Murray, J.M., Appleton, P.L., Swedlow, J.R. & Waters, J.C. (2007) Evaluating performance in three-dimensional fluorescence microscopy. *Journal of Microscopy*, **228**, 390–405.

Myers, G. (2012) Why bioimage informatics matters. *Nature Methods*, **9**, 659–660.

Nagy, J.G. & O'Leary, D.P. (1997) Fast iterative image restoration with a spatially varying PSF., pp. 388–399.

Nanguneri, S., Flottmann, B., Horstmann, H., Heilemann, M. & Kuner, T. (2012) Three-Dimensional, Tomographic Super-Resolution Fluorescence Imaging of Serially Sectioned Thick Samples. *PLoS ONE*, **7**, e38098.

Neil, M.A.A., Juskaitis, R. & Wilson, T. (1997) Method of obtaining optical sectioning by using structured light in a conventional microscope. *Optics Letters*, **22**, 1905.

Neil, M.A.A., Juškaitis, R. & Wilson, T. (1998) Real time 3D fluorescence microscopy by two beam interference illumination. *Optics Communications*, **153**, 1–4.

Neumann, B., Walter, T., Hériché, J.-K., Bulkescher, J., Erfle, H., Conrad, C., Rogers, P., Poser, I., Held, M., Liebel, U., Cetin, C., Sieckmann, F., Pau, G., Kabbe, R., Wünsche, A., Satagopam, V., Schmitz, M.H.A., Chapuis, C., Gerlich, D.W., Schneider, R., Eils, R., Huber, W., Peters, J.-M., Hyman, A.A., Durbin, R., Pepperkok, R. & Ellenberg, J. (2010) Phenotypic profiling of the human genome by time-lapse microscopy reveals cell division genes. *Nature*, **464**, 721–727.

Odermatt, P.D., Shivanandan, A., Deschout, H., Jankele, R., Nievergelt, A.P., Feletti, L., Davidson, M.W., Radenovic, A. & Fantner, G.E. (2015) High-Resolution Correlative Microscopy: Bridging the Gap between Single Molecule Localization Microscopy and Atomic Force Microscopy. *Nano Letters*, **15**, 4896–4904.

Osada, T., Uehara, H., Kim, H. & Ikai, A. (2003) mRNA analysis of single living cells. *Journal of Nanobiotechnology*, **1**, 2.

Paul, P., Kalamatianos, D., Duessmann, H. & Huber, H. (2008) Automatic quality assessment for fluorescence microscopy images. *8th IEEE International Conference on BioInformatics and BioEngineering, 2008. BIBE 2008*, pp. 1–6.

Prabhakar, N., Peurla, M., Koho, S., Deguchi, T., Hänninen, P. & Rosenholm, J.

(Unpublished) Nanodiamonds as multi-modal probes in super-resolution STED-TEM correlative microscopy.

Preibisch, S., Amat, F., Stamataki, E., Sarov, M., Singer, R.H., Myers, E. & Tomancak, P. (2014) Efficient Bayesian-based multiview deconvolution. *Nature Methods*, **11**, 645–648.

Preibisch, S., Saalfeld, S., Schindelin, J. & Tomancak, P. (2010) Software for bead-based registration of selective plane illumination microscopy data. *Nature Methods*, **7**, 418–419.

Preibisch, S., Saalfeld, S. & Tomancak, P. (2009) Globally optimal stitching of tiled 3D microscopic image acquisitions. *Bioinformatics*, **25**, 1463–1465.

Preza, C., Miller, M.I., Thomas, Jr., L.J. & McNally, J.G. (1992) Regularized linear method for reconstruction of three-dimensional microscopic objects from optical sections. *Journal of the Optical Society of America A*, **9**, 219.

Punge, A., Rizzoli, S.O., Jahn, R., Wildanger, J.D., Meyer, L., Schönle, A., Kastrup, L. & Hell, S.W. (2008) 3D reconstruction of high-resolution STED microscope images. *Microscopy research and technique*, **71**, 644–650.

Redondo, R., Bueno, G., Cristóbal, G., Vidal, J., Déniz, O., García-Rojo, M., Murillo, C., Relea, F. & González, J. (2012) Quality evaluation of microscopy and scanned histological images for diagnostic purposes. *Micron*, **43**, 334–343.

Rego, E.H., Shao, L., Macklin, J.J., Winoto, L., Johansson, G.A., Kamps-Hughes, N., Davidson, M.W. & Gustafsson, M.G.L. (2012) Nonlinear structured-illumination microscopy with a photoswitchable protein reveals cellular structures at 50-nm resolution. *Proceedings of the National Academy of Sciences*, **109**, E135–E143.

Remmele, S., Oehm, B., Staier, F., Eipel, H., Cremer, C. & Hesser, J. (2011) Reconstruction of high-resolution fluorescence microscopy images based on axial tomography. *Proceedings of SPIE 7692*, p. 79624O–79624O–10.

Renaud, O., Viña, J., Yu, Y., Machu, C., Trouvé, A., Van der Voort, H., Chalmond, B. & Shorte, S.L. (2008) High-resolution 3-D imaging of living cells in suspension using confocal axial tomography. *Biotechnology Journal*, **3**, 53–62.

Richardson, W.H. (1972) Bayesian-Based Iterative Method of Image Restoration. *Journal of the Optical Society of America*, **62**, 55–59.

Rust, M.J., Bates, M. & Zhuang, X. (2006) Sub-diffraction-limit imaging by stochastic optical reconstruction microscopy (STORM). *Nature Methods*, **3**, 793–796.

Sandison, D.R., Piston, D.W., Williams, R.M. & Webb, W.W. (1995) Quantitative comparison of background rejection, signal-to-noise ratio, and resolution in confocal and full-field laser scanning microscopes. *Applied Optics*, **34**, 3576.

Sarder, P. & Nehorai, A. (2006) Deconvolution methods for 3-D fluorescence microscopy images. *IEEE Signal Processing Magazine*, **23**, 32–45.

Sätzler, K. & Eils, R. (1997) Resolution improvement by 3-D reconstructions from tilted views in axial tomography and confocal theta microscopy. *Bioimaging*, **5**, 171–182.

Saux, B.L., Chalmond, B., Yu, Y., Trouvé, A., Renaud, O. & Shorte, S. l. (2009) Isotropic high-resolution three-dimensional confocal micro-rotation imaging for non-adherent living cells. *Journal of Microscopy*, **233**, 404–416.

Schindelin, J., Arganda-Carreras, I., Frise, E., Kaynig, V., Longair, M., Pietzsch, T., Preibisch, S., Rueden, C., Saalfeld, S., Schmid, B., Tinevez, J.-Y., White, D.J., Hartenstein, V., Eliceiri, K., Tomancak, P. & Cardona, A. (2012) Fiji: an open-source platform for biological-image analysis. *Nature Methods*, **9**, 676–682.

Schmid, B. & Huisken, J. (2015) Real-time multi-view deconvolution. *Bioinformatics*, btv387.

Schmid, B., Schindelin, J., Cardona, A., Longair, M. & Heisenberg, M. (2010) A high-level 3D visualization API for Java and ImageJ. *BMC Bioinformatics*, **11**, 274.

Schmidt, R., Wurm, C.A., Jakobs, S., Engelhardt, J., Egner, A. & Hell, S.W. (2008) Spherical nanosized focal spot unravels the interior of cells. *Nature Methods*, **5**, 539–544.

Schneider, J., Zahn, J., Maglione, M., Sigrist, S.J., Marquard, J., Chojnacki, J., Kräusslich, H.-G., Sahl, S.J., Engelhardt, J. & Hell, S.W. (2015) Ultrafast, temporally stochastic STED nanoscopy of millisecond dynamics. *Nature Methods*, **advance online publication**.

Shamir, L., Delaney, J.D., Orlov, N., Eckley, D.M. & Goldberg, I.G. (2010) Pattern Recognition Software and Techniques for Biological Image Analysis. *PLoS Comput Biol*, **6**, e1000974.

Shariff, A., Kangas, J., Coelho, L.P., Quinn, S. & Murphy, R.F. (2010) Automated Image Analysis for High-Content Screening and Analysis. *Journal of Biomolecular Screening*, **15**, 726–734.

Shaw, P.J. (1990) Three-dimensional optical microscopy using tilted views. *Journal of Microscopy*, **158**, 165–172.

Shaw, P. (1994) Deconvolution in 3-D optical microscopy. *The Histochemical Journal*, **26**, 687–694.

Shaw, P.J. (2006) Comparison of Widefield/Deconvolution and Confocal Microscopy for Three-Dimensional Imaging. *Handbook Of Biological Confocal Microscopy* (ed J.B. Pawley), pp. 453–467. Springer US.

Shaw, P.J., Agard, D.A., Hiraoka, Y. & Sedat, J.W. (1989) Tilted view reconstruction in optical microscopy. Three-dimensional reconstruction of Drosophila melanogaster embryo nuclei. *Biophysical Journal*, **55**, 101–110.

Sheppard, C.J.R., Gan, X., Gu, M. & Roy, M. (2006) Signal-to-Noise Ratio in Confocal Microscopes. *Handbook Of Biological Confocal Microscopy* (ed J.B. Pawley), pp. 442–452. Springer US.

Shtengel, G., Galbraith, J.A., Galbraith, C.G., Lippincott-Schwartz, J., Gillette, J.M., Manley, S., Sougrat, R., Waterman, C.M., Kanchanawong, P., Davidson, M.W., Fetter, R.D. & Hess, H.F. (2009) Interferometric fluorescent super-resolution microscopy resolves 3D cellular ultrastructure. *Proceedings of the National Academy of Sciences*, **106**, 3125–3130.

Spiegelhalter, C., Laporte, J.F. & Schwab, Y. (2014) Correlative Light and Electron Microscopy: From Live Cell Dynamic to 3D Ultrastructure - Springer., Methods in Molecular Biology (ed J. Kuo) Humana Press.

Stelzer, E.H.K. & Lindek, S. (1994) Fundamental reduction of the observation volume in far-field light microscopy by detection orthogonal to the illumination axis: confocal theta microscopy. *Optics Communications*, **111**, 536–547.

Swoger, J., Huisken, J. & Stelzer, E.H.K. (2003) Multiple imaging axis microscopy improves resolution for thick-sample applications. *Optics Letters*, **28**, 1654.

Swoger, J., Verveer, P., Greger, K., Huisken, J. & Stelzer, E.H.K. (2007) Multi-view image fusion improves resolution in three-dimensional microscopy. *Optics Express*, **15**, 8029–8042.

Tang, J., Akerboom, J., Vaziri, A., Looger, L.L. & Shank, C.V. (2010) Near-isotropic 3D optical nanoscopy with photon-limited chromophores. *Proceedings of the National Academy of Sciences of the United States of America*, **107**, 10068–10073.

Temerinac-Ott, M., Ronneberger, O., Ochs, P., Driever, W., Brox, T. & Burkhardt, H. (2012) Multiview Deblurring for 3-D Images from Light-Sheet-Based Fluorescence Microscopy. *IEEE Transactions on Image Processing*, **21**, 1863–1873.

Theer, P., Hasan, M.T. & Denk, W. (2003) Two-photon imaging to a depth of 1000 μm in living brains by use of a Ti:Al_2O_3 regenerative amplifier. *Optics Letters*, **28**, 1022.

The quest for quantitative microscopy (Editorial). (2012) *Nature Methods*, **9**, 627–627.

Thevenaz, P., Ruttimann, U.E. & Unser, M. (1998) A pyramid approach to subpixel registration based on intensity. *Image Processing, IEEE Transactions on*, **7**, 27–41.

Thompson, R.E., Larson, D.R. & Webb, W.W. (2002) Precise nanometer localization analysis for individual fluorescent probes. *Biophysical Journal*, **82**, 2775–2783.

Tikhonov, A.N. & Arsenin, V.Y. (1977) *Solutions of Ill-Posed Problems*. Wiley.

Tomer, R., Khairy, K., Amat, F. & Keller, P.J. (2012) Quantitative high-speed imaging of entire developing embryos with simultaneous multiview light-sheet microscopy. *Nature Methods*, **9**, 755–763.

Van Der Voort, H.T.M. & Strasters, K.C. (1995) Restoration of confocal images for quantitative image analysis. *Journal of Microscopy*, **178**, 165–181.

Van Kempen & Van Vliet. (2000) The influence of the regularization parameter and the first estimate on the performance of Tikhonov regularized non-linear image restoration algorithms. *Journal of Microscopy*, **198**, 63–75.

Verveer, P.J., Gemkow, M.J. & Jovin, T.M. (1999) A comparison of image restoration approaches applied to three-dimensional confocal and wide-field fluorescence microscopy. *Journal of Microscopy*, **193**, 50–61.

Verveer, P.J., Swoger, J., Pampaloni, F., Greger, K., Marcello, M. & Stelzer, E.H.K. (2007) High-resolution three-dimensional imaging of large specimens with light sheet–based

microscopy. *Nature Methods*, **4**, 311–313.

Vicidomini, G., Moneron, G., Han, K.Y., Westphal, V., Ta, H., Reuss, M., Engelhardt, J., Eggeling, C. & Hell, S.W. (2011) Sharper low-power STED nanoscopy by time gating. *Nat Meth*, **8**, 571–573.

Voie, A.H., Burns, D.H. & Spelman, F.A. (1993) Orthogonal-plane fluorescence optical sectioning: three-dimensional imaging of macroscopic biological specimens. *Journal of microscopy*, **170**, 229–236.

Wang, K., Milkie, D.E., Saxena, A., Engerer, P., Misgeld, T., Bronner, M.E., Mumm, J. & Betzig, E. (2014) Rapid adaptive optical recovery of optimal resolution over large volumes. *Nature Methods*, **11**, 625–628.

Watanabe, S., Punge, A., Hollopeter, G., Willig, K.I., Hobson, R.J., Davis, M.W., Hell, S.W. & Jorgensen, E.M. (2011) Protein localization in electron micrographs using fluorescence nanoscopy. *Nature Methods*, **8**, 80–84.

Waters, J.C. (2007) Live-Cell Fluorescence Imaging. *Methods in Cell Biology*, Digital Microscopy, 3rd Edition (ed G.S. and D.E. Wolf), pp. 115–140. Academic Press.

Waters, J.C. (2009) Accuracy and precision in quantitative fluorescence microscopy. *The Journal of Cell Biology*, **185**, 1135–1148.

Wildanger, D., Medda, R., Kastrup, L. & Hell, S. w. (2009) A compact STED microscope providing 3D nanoscale resolution. *Journal of Microscopy*, **236**, 35–43.

Willig, K.I., Harke, B., Medda, R. & Hell, S.W. (2007) STED microscopy with continuous wave beams. *Nature Methods*, **4**, 915–918.

Wilson, T. (2011) Resolution and optical sectioning in the confocal microscope. *Journal of Microscopy*, **244**, 113–121.

Wilson, T. & Carlini, A.R. (1988) Three-dimensional imaging in confocal imaging systems with finite sized detectors. *Journal of Microscopy*, **149**, 51–66.

Wojcik, M., Hauser, M., Li, W., Moon, S. & Xu, K. (2015) Graphene-enabled electron microscopy and correlated super-resolution microscopy of wet cells. *Nature Communications*, **6**.

Yildiz, A. & Selvin, P.R. (2005) Fluorescence imaging with one nanometer accuracy: application to molecular motors. *Accounts of Chemical Research*, **38**, 574–582.

Yoo, T.S., Ackerman, M.J., Lorensen, W.E., Schroeder, W., Chalana, V., Aylward, S., Metaxas, D. & Whitaker, R. (2002) Engineering and algorithm design for an image processing Api: a technical report on ITK--the Insight Toolkit. *Studies in health technology and informatics*, **85**, 586–592.

Yu, Y., Trouvé, A., Chalmond, B., Renaud, O. & Shorte, S.L. (2011) Confocal bi-protocol: a new strategy for isotropic 3D live cell imaging. *Journal of Microscopy*, **242**, 70–85.